

Numerical simulation of three-fluid Rayleigh-Taylor instability using an enhanced Volume-Of-Fluid (VOF) model: New benchmark solutions

Faroogh Garoosi^{*}, Tew-Fik Mahdi

Department of Civil, Geological and Mining Engineering, Polytechnique Montreal, University of Montreal Campus, 2900 boul. Edouard-Montpetit, Montreal, QC H3T 1J4, Canada



ARTICLE INFO

Keywords:

High-order TVD-NVD advection scheme
Hybrid PISO-SIMPLEC algorithm
Multi-fluid flows
PLIC-ELVIRA technique
Improved VOF model
Rayleigh-Taylor instability

ABSTRACT

The main objective of the present study is to introduce two novel benchmark solutions namely: two-dimensional three-fluid Rayleigh-Taylor Instability problems, aiming to provide an up-to-date data set and a unique fundamental insight into morphology and hydrodynamic behavior of coupled Rayleigh-Taylor-Kelvin-Helmholtz instability phenomenon. To this end, the Volume-Of-Fluid (VOF) model is adopted to probe the complex configurations and kinetic processes of highly nonlinear multi-fluid flow problems with large topological changes and moving interfaces. However, to improve the performance and accuracy of the classical VOF model and preserve monotonicity for the density and viscosity, a novel high-order bounded advection scheme is first proposed in the context of the Total Variation Diminishing and Normalized Variable Diagram (TVD-NVD) constraints and then is utilized for the discretization of the convection terms in the Navier-Stokes and transport equations. To further increase the accuracy of the numerical simulations, the second-order PLIC-ELVIRA is implemented for the reconstruction of the physical discontinuity between phases and the determination of its curvature. Furthermore, to enhance the consistency and stability of the classical VOF model in handling incompressible multi-fluid flows, a novel semi-iterative pressure-velocity coupling algorithm is constructed by the combination of the standard PISO and SIMPLEC algorithms and is then applied to ensure mass conservation in each grid cell. To demonstrate the versatility and robustness of the proposed model in dealing with the multiphase flows involving large interface deformation and breaking phenomena, a series of canonical test cases such as dam-break over a dry bed with and without stationary obstacle, 2D three-fluid rising bubble, two-fluid and three-fluid Rayleigh-Taylor Instability are adopted. In the last stage, an improved VOF model is applied to solve two new three-fluid Rayleigh-Taylor Instability benchmark problems on a staggered grid system. The results of this study can provide a wide panorama on the improvements of standard VOF model and may be utilized as benchmark solutions for validation of various CFD tools or simply to understand more complex related multi-fluid flows.

1. Introduction

Incompressible multi-fluid and multiphase flows occur ubiquitously in nature, medical processes and engineering systems [1]. Examples include nuclear and chemical reactors [2,3], melting and solidification [4,5], gas-liquid fluidized bed reactor [6], fuel injection and spray atomization [7,8], irrigation and water allocation [9], topical drug delivery [10,11] and so on. During the last two decades, owing to rapid advancement in computer technology and numerical algorithms, the implementation of the Computational Fluid Dynamics (CFD) as a promising and cost-effective alternative to the conventional approaches

(i.e. experimental and analytical solutions) has attracted a great deal of attention among the engineering and scientific communities [12]. Conversely, the development of reliable and robust multiphase computational methodologies is still ongoing and their industrial use is mostly restricted to simple configurations [13]. Being the mainstream approaches, the Level-Set (LS) [14] and Volume-Of-Fluid (VOF) [15] as two popular and widely used interface-capturing techniques have proven to be very efficient for the investigation and understanding the underlying physics behind the multiphase flows. The simulations of landslide-induced tsunamis [16], bubble rising [17–19], dam failure problem [20–22], droplet impact on solid surface [23,24], wave and structure interaction (i.e. FSI) [25–27] are just a few examples of such

* Corresponding author.

E-mail addresses: faroogh.garoosi@polymtl.ca (F. Garoosi), tewfik.mahdi@polymtl.ca (T.-F. Mahdi).

Nomenclature		
C_φ	Interface compression coefficient	
F_g	gravity force	
F_{ST}	surface tension force	
g	Gravitational acceleration, $m s^{-2}$	
H	enclosure height, m	
L	Length of the enclosure (m)	
\hat{n}	interface normal vector	
p	pressure, N/m^2	
P	dimensionless pressure	
ttime (s)	time (s)	
T	dimensionless time, ($T = t\sqrt{g/H}$)	
u, v	velocity components, m/s	
u_R	artificial compressive velocity, m/s	
Re	Reynolds number	
U, V	Dimensionless velocity components	
x, y	Cartesian coordinates, m	
		X, Y Dimensionless Cartesian coordinates
		We Weber number
<i>Greek symbols</i>		
μ dynamic viscosity, kg/ms		
ν kinematic viscosity $y, m^2/s$		
ρ density, kg/m^3		
φ Volume fraction of the primary phase (phase 1)		
λ Volume fraction of the secondary phase (phase 2)		
γ Volume fraction of the third phase (phase 3)		
\tilde{k} curvature of interface		
σ interfacial tension coefficient		
ψ stream function($= - \int_{Y_0}^Y U \partial Y + \psi(X, Y_0)$)		
<i>Subscripts</i>		
L Lighter fluid		
H Heavy fluid		
M Middle fluid		

studies in which LS and VOF models were adopted to predict the hydrodynamics and morphological changes of transport problems. A state-of-the-art literature review concerning recent applications of LS and VOF can be found in works of Saye et al. [28] and Marić et al. [29].

However, the results of Zuzio et al. [30] showed that, although these two models have demonstrated to be robust and flexible enough to capture complex topological changes, they are characterized by some crucial shortcoming which can immensely hinder their further applications as means of CFD calculations. To be more precise, the former approach uses an explicit regularized (smooth) version of the Heaviside function to determine the position and curvature of the interface. Despite its efficiency in calculating the geometrical information of the interface, the Level-Set model is not conservative in nature and suffers from the lack of conservation of mass unless fine grids are used [31]. On the other hand, although the VOF method can successfully guarantee the global mass conservation by construction, it is characterized by false-diffusion errors and unphysical growth of physical discontinuity which in turn lead to the interface smearing and spurious velocity/pressure fluctuations in the region where sharp gradients exist (e.g. density/viscosity jumps) [32,33]. Accompanied by this drawback, the VOF is, in general, less accurate in predicting the geometrical quantities of the interface such that the special interface reconstruction technique is required to retrieve and identify the interface orientation and its normal vector [34,35]. Over the last decades, considerable attempts have been devoted to address the aforementioned problems and improve the stability and consistency of the VOF model.

To minimize excessive computational smearing and mitigate undesirable effects of numerical diffusion, in pioneering work, Gaskell and Lau [36] and Leonard [37] have introduced the notion of Normalized Variable Diagram (NVD) and Convection Boundedness Criterion (CBC). They proposed a novel Simple High-Accuracy Resolution Program (SHARP) scheme for the treatment of the advection term in transport equation and concluded that contrary to the classical QUICK and second-order Upwind scheme, the SHARP model can successfully guarantee conservativeness of the numerical solution while maintaining the boundedness of a convected scalar transport variable in the vicinity of steep gradients and material discontinuities. Another important restricting criterion and clarifying tool was also introduced by Harten

[38] and Sweby [39] who independently proposed the idea of a non-oscillatory flux-limiter function known as TVD (Total Variational Diminishing) schemes. Later, Lin [40] mathematically proved that, the TVD constraints are more restrictive than the CBC conditions and pointed out that the CBC condition cannot solely guarantee iterative convergence and monotonicity of the solution. Similar finding were also reported by Alves et al. [41], Chourushi [42] and Lima et al. [43] and Gao et al. [44] who analytically showed that, the NVD schemes may be unbounded and are susceptible to numerical instability which manifest itself through spurious overshoots and undershoots in the volume-fraction field during the transitional stage (i.e. $\varphi > 1$ or $\varphi < 0$). Since then, various schemes were constructed based on the NVD, CBC and TVD constraints such as SOUCUP, HLPA, SMARTER and LPPA, SMART for the simulation of the convection-dominated problems [45]. In the same context, Ubbink and Issa [46] showed that, the aforementioned high resolution differencing schemes require adaptive under relaxation parameters for the pressure and momentum terms which in turn can slow down the convergence of the computation and impose an additional limitation to their use in the highly non-linear flows. To overcome this deficiency, they developed a hybrid NVD discretisation scheme called CICSAM (Compressive Interface Capturing Scheme for Arbitrary Meshes) and asserted that, the CICSAM can efficiently ensure boundedness of the volume fraction field and is flexible enough to be extended to the unstructured meshes. Recently, Gopala et al. [47], Zhang et al. [48], Nguyen et al. [49], Wacławczyk et al. [50], however, questioned the reliability and feasibility of the implicit CICSAM scheme in dealing with the complex multiphase flows involving interface merging or break-up. They stressed that, this scheme is characterized by the formation of the non-physical “Jetsam” and “Flotsam” phenomena and cannot produce monotonic profiles of the color function, leading to the smearing of the interface properties. An alternative treatment to preserve interface sharpness and suppress smearing the information at the physical discontinuities was then proposed by Heyns et al. [51] who established the idea of Artificial Compressive Technique (ACT) by embedding the additional gradient terms into the transport equation. This technique was then extended and employed by Cifani et al. [52], Zanotto et al. [53], Akhlaghi et al. [54] and Peng et al. [55] for the simulation of challenging real-life problems such as slurry Taylor flow,

bubble rising and CFD-DEM. They concluded that, this technique can efficiently eliminate the detrimental effects of false-diffusion errors, thereby maintaining the integrity and shape of interface.

Referring to the second deficiency associated with velocity/pressure fluctuations across the moving interfaces, Habchi et al. [56], Sarath et al. [57], Introini et al. [58] and Kim et al. [59] employed the merged version of PISO [60] and SIMPLE [61] algorithms so-called “PIMPLE” (available in OpenFOAM® platform) to solve the pressure-velocity

coupling and speed up the convergence rate of calculations. Their results revealed that, the implementation of the PIMPLE algorithm results in relatively smoother pressure fields especially when simulations with large time steps are of interest. Furthermore, they found that, unlike the sole PISO or SIMPLE algorithm, PIMPLE is less sensitive to numerical instability, making it more suitable for strongly coupled problems where the use of an explicit temporal discretization may demand small time step to keep the simulation stable. However, the comprehensive

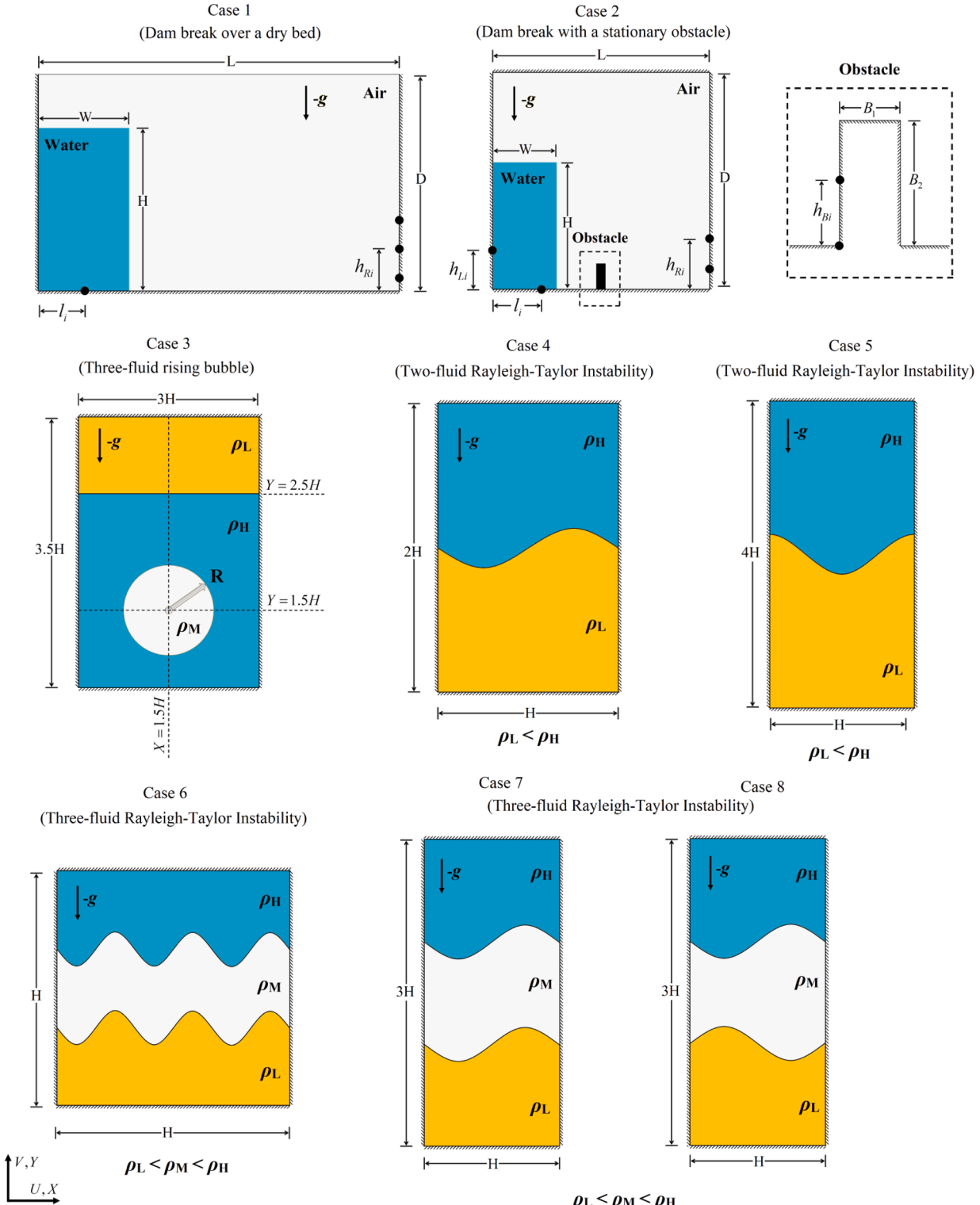


Fig. 1. Schematic diagram of eight different physical models under consideration with associated boundary conditions and coordinate system.

literature review on five different pressure-based solvers conducted by Wang et al. [33] showed, due to the existence of the additional iterative loop in PIMPLE algorithm, the methodology is not computationally affordable when it will be applied to the large scale three-dimensional problems.

Finally, as mentioned earlier, contrary to Level-Set model, the third challenge faced by VOF is to determine the geometrical quantities of the interface for the accurate imposition of surface tension force. To circumvent this issue, Youngs [62] invented the first-order accurate interface reconstruction technique defined in the 3×3 grid stencils and later pioneered the concept of Piecewise Line Interface Construction (PLIC). However, Pilliod et al. [35] analytical proved that, Youngs' formulations fails to exactly reproduce all linear interface and is prone to fragment a smooth front. To remedy this defect, they proposed the ELVIRA method and mathematically showed that, this iterative technique can effectively reconstruct the linear interface and benefits from the second-order of accuracy. The ELVIRA was then elaborated in details and adopted by Garoosi et al. [63] for modelling of multi-fluid flows with large deformation and fragmentation.

In light of the above literature survey, one can deduce that there are still three crucial shortcomings associated with interface-capturing VOF model including (1) the interface smearing arising from the false-diffusion errors, (2) non-physical pressure/velocity fluctuations across the material discontinuities owing to the deficiency in existing pressure-based solvers, and (3) the reconstruction of the interface and calculation of its curvature for the accurate imposition of the surface tension force, which in turns can jeopardize the reliability and accuracy of the simulations or even lead to the premature termination of the calculations. Thus, the focus of the current work is to address the above drawbacks systematically, aiming to establish an enhanced version of the VOF model for the simulation of multi-fluid and free-surface flows. To accomplish this objective, a novel third-order bounded advection scheme is first constructed based on the hybrid TVD-NVD constraints and is then applied for the discretization of the convection terms in the governing equations (see Section 4). To further control the unphysical growth of interface thickness and limit the interfacial zone to the minimum number of grid spacing, the artificial compression velocity term (ACT) is also added into the volume-fraction equation(s). In order to improve the stability of the solution at a reasonable computational cost, the semi-iterative pressure-based algorithm is developed by the combination of the PISO and SIMPLC algorithms and then utilized for the treatment of the pressure-velocity coupling (see Appendix A). To reconstruct the interface and extract the geometrical information, the ELVIRA technique is coded and then applied into the momentum equations. The ELVIRA technique coded in FORTRAN language is also provided in supplementary material as the subroutine. The validity of the proposed modifications is demonstrated against the six challenging benchmark cases including dam-break over a dry bed with and without stationary obstacle, single bubble rising and Rayleigh-Taylor Instability problems (see Section 5). In the last stage, two novel benchmark cases (i. e. 2D three-fluid Rayleigh-Taylor Instability) are also introduced and analyzed by the verified VOF model, aiming to provide an up-to-date data set and a unique fundamental insight into morphology and hydrodynamic behavior of coupled Rayleigh-Taylor-Kelvin-Helmholtz instability phenomena (see Section 6).

2. Problem statement and governing equations

Schematic diagram of the physical models considered in the current work along with the corresponding boundary conditions are depicted in Fig. 1 where cases 1 to 6 are used for validation and verification of the proposed modifications in handling multi-fluid flow problems, whereas cases 7 and 8 are introduced as two novel benchmark solutions to generate a state-of-the-art three-fluid Rayleigh-Taylor Instability dataset and useful resources for testing and validating both traditional and modern numerical models. All simulations were conducted in the Fortran 90 programming language and the developed code was compiled using the Intel® Visual FORTRAN Compiler 19.0. The set of governing equations including continuity, momentum, and volume fraction for unsteady, laminar, incompressible and Newtonian fluid flows may be expressed as follows [46,64]:

$$\frac{\partial \rho}{\partial t} + \frac{\partial \rho u}{\partial x} + \frac{\partial \rho v}{\partial y} = 0, \quad (1)$$

$$\frac{\partial \rho_m u}{\partial t} + \frac{\partial \rho_m uu}{\partial x} + \frac{\partial \rho_m vu}{\partial y} = -\frac{\partial p}{\partial x} + \left[\frac{\partial}{\partial x} \mu_m \left(\frac{\partial u}{\partial x} \right) + \frac{\partial}{\partial y} \mu_m \left(\frac{\partial u}{\partial y} \right) \right] + F_{ST,i} \quad (2)$$

$$\frac{\partial \rho_m v}{\partial t} + \frac{\partial \rho_m uv}{\partial x} + \frac{\partial \rho_m vv}{\partial y} = -\frac{\partial p}{\partial y} + \left[\frac{\partial}{\partial x} \mu_m \left(\frac{\partial v}{\partial x} \right) + \frac{\partial}{\partial y} \mu_m \left(\frac{\partial v}{\partial y} \right) \right] + \rho_m g + F_{ST,i} \quad (3)$$

$$\frac{\partial \varphi}{\partial t} + \frac{\partial \varphi u}{\partial x} + \frac{\partial \varphi v}{\partial y} + \nabla \cdot (\varphi (1-\varphi) \mathbf{u}_{R\varphi}) = 0 \quad (4)$$

$$\frac{\partial \lambda}{\partial t} + \frac{\partial \lambda u}{\partial x} + \frac{\partial \lambda v}{\partial y} + \nabla \cdot (\lambda (1-\lambda) \mathbf{u}_{R\lambda}) = 0 \quad (5)$$

$$\varphi + \lambda + \gamma = 1 \quad (6)$$

In the above equations, u and v are the dimensional mixture velocities in x and y -directions while the terms g and p represent gravity acceleration and pressure, respectively. ρ_m and μ_m denote averaged density and dynamic viscosity of immiscible working fluids which may be approximated linearly by Soh et al. [65]:

$$\rho_m = \varphi \rho_1 + (1-\varphi) \rho_2 \quad (7)$$

$$\mu_m = \varphi \mu_1 + (1-\varphi) \mu_2 \quad (8)$$

$$\rho_m = \varphi \rho_1 + \lambda \rho_2 + (1-\lambda-\varphi) \rho_3 \quad (9)$$

$$\mu_m = \varphi \mu_1 + \lambda \mu_2 + (1-\lambda-\varphi) \mu_3 \quad (10)$$

where Eqs. (7) and (8) are used for estimating the physical properties of two-fluid flows whereas Eqs. (9) and (10) are exploited for three-fluid problems. In the above equations, the subscripts 1, 2 and 3 refer to the fluid-components involved in the problem. The term $F_{ST,i}$ in the momentum equations represents volumetric surface tension force which acts only in the vicinity of the material interfaces ($0 < \varphi < 1, 0 < \lambda < 1$ and $0 < \gamma < 1$) according to Brackbill's model [66] given by:

$$F_{ST,\varphi} = \sigma_\varphi \tilde{k}_\varphi \nabla \varphi, \quad (11)$$

$$F_{ST,\lambda} = \sigma_\lambda \tilde{k}_\lambda \nabla \lambda,$$

where σ_i represents the interfacial tension coefficient between working fluids and \tilde{k}_i is the curvature of interface in a computational cell defined

as [67]:

$$\begin{aligned}\tilde{k}_\varphi &= -\nabla \cdot \hat{\mathbf{n}}_\varphi = -\nabla \cdot \left(\frac{\nabla \varphi}{|\nabla \varphi|} \right), \\ \tilde{k}_\lambda &= -\nabla \cdot \hat{\mathbf{n}}_\lambda = -\nabla \cdot \left(\frac{\nabla \lambda}{|\nabla \lambda|} \right),\end{aligned}\quad (12)$$

$$\begin{aligned}\hat{\mathbf{n}}_\varphi &= \frac{\vec{n}_\varphi}{|\vec{n}_\varphi|}, \quad \vec{n}_\varphi = \nabla \varphi, \\ \hat{\mathbf{n}}_\lambda &= \frac{\vec{n}_\lambda}{|\vec{n}_\lambda|}, \quad \vec{n}_\lambda = \nabla \lambda,\end{aligned}\quad (13)$$

where $\hat{\mathbf{n}}$ denotes interface normal vector which is non-zero only at the interface. The third term ($\nabla \cdot (\varphi(1-\varphi)\mathbf{u}_{R\varphi})$ and $\nabla \cdot (\lambda(1-\lambda)\mathbf{u}_{R\lambda})$) in Eqs. (4) and (5) are the artificial compression velocity [51–53] which helps in preserving the sharpness of the interface region. Note that, the existence of variables $\varphi(1-\varphi)$ and $\lambda(1-\lambda)$ in the aforementioned equations ensures that the compression terms are active only adjacent to the interface region. \mathbf{u}_R is the compressive velocity which is formulated based on maximum velocity magnitude in the interface region as [54]:

$$\mathbf{u}_{R\varphi} = C_\varphi |\vec{u}| \hat{\mathbf{n}}_\varphi = C_\varphi |\vec{u}| \frac{\nabla \varphi}{|\nabla \varphi|}, \quad (14)$$

$$\mathbf{u}_{R\lambda} = C_\lambda |\vec{u}| \hat{\mathbf{n}}_\lambda = C_\lambda |\vec{u}| \frac{\nabla \lambda}{|\nabla \lambda|},$$

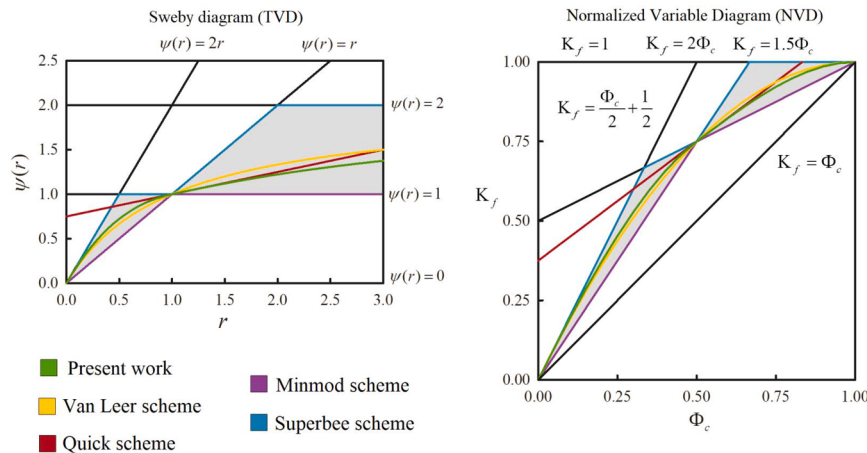
The coefficient $C_\varphi = C_\lambda = 0.5$ is the primary parameter which controls the compression of the interface [55,68].

Before closing this section, it is interesting to mention that, the proposed VOF model can be extended to the more than three immiscible working fluids in three-dimensional problems. For example, in the case of four fluids, the transport equations (Eqs. (4)–(6)) in three-dimensional form in the Cartesian coordinate system may be written as:

$$\frac{\partial \varphi}{\partial t} + \frac{\partial \varphi u}{\partial x} + \frac{\partial \varphi v}{\partial y} + \frac{\partial \varphi w}{\partial z} + \nabla \cdot (\varphi(1-\varphi)\mathbf{u}_{R\varphi}) = 0 \quad (15)$$

$$\frac{\partial \lambda}{\partial t} + \frac{\partial \lambda u}{\partial x} + \frac{\partial \lambda v}{\partial y} + \frac{\partial \lambda w}{\partial z} + \nabla \cdot (\lambda(1-\lambda)\mathbf{u}_{R\lambda}) = 0 \quad (16)$$

$$\frac{\partial \gamma}{\partial t} + \frac{\partial \gamma u}{\partial x} + \frac{\partial \gamma v}{\partial y} + \frac{\partial \gamma w}{\partial z} + \nabla \cdot (\gamma(1-\gamma)\mathbf{u}_{R\gamma}) = 0 \quad (17)$$



The u -control volume and its neighbouring velocity components

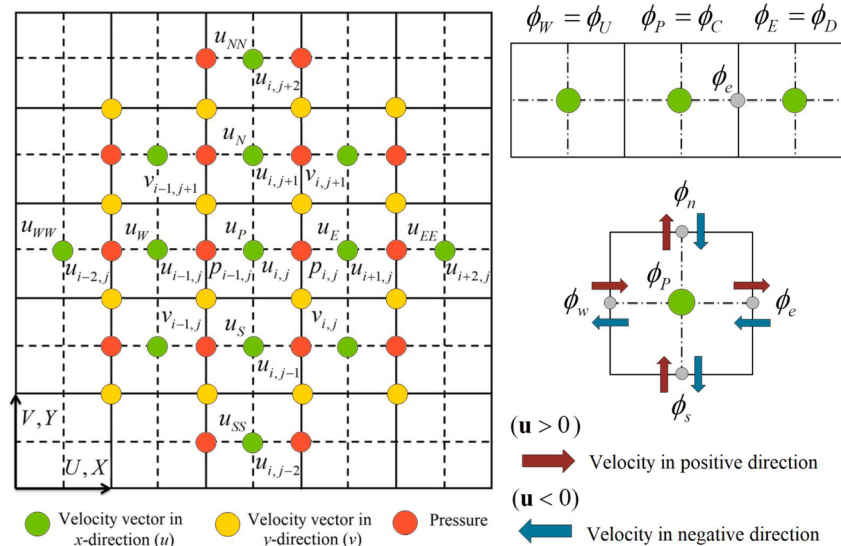


Fig. 2. (a) Sweby and Normalized Variable diagrams showing the proposed model along with the four other well-known convection schemes (the shaded areas convey the TVD region). (b) The 2D staggered grid arrangement used for discretization of the proposed scheme.

$$\beta = 1 - \varphi - \lambda - \gamma \quad (18)$$

where φ, λ, γ and β are the volume fractions of the first, second, third and fourth working fluids. At this stage, it is worthwhile mentioning that, in order to decrease the computational cost, Eq. (18) is typically utilized to determine the volume fraction of the fourth fluid. However, instead of Eq. (18), the following equation can be used interchangeably in the CFD code:

$$\frac{\partial \beta}{\partial t} + \frac{\partial \beta u}{\partial x} + \frac{\partial \beta v}{\partial y} + \frac{\partial \beta w}{\partial z} + \nabla \cdot (\beta (1 - \beta) \mathbf{u}_{R\beta}) = 0 \quad (19)$$

As stated earlier, in the above equation, the variables $\mathbf{u}_{R\varphi}$, $\mathbf{u}_{R\lambda}$, $\mathbf{u}_{R\gamma}$ and $\mathbf{u}_{R\beta}$ are the compressive velocity which can be approximated based on maximum velocity magnitude in the interface area as:

$$\mathbf{u}_{R\varphi} = C_\varphi |\vec{u}| \hat{\mathbf{n}} = C_\varphi |\vec{u}| \frac{\nabla \varphi}{|\nabla \varphi|}, \quad (20)$$

$$\mathbf{u}_{R\lambda} = C_\lambda |\vec{u}| \hat{\mathbf{n}} = C_\lambda |\vec{u}| \frac{\nabla \lambda}{|\nabla \lambda|},$$

$$\mathbf{u}_{R\gamma} = C_\gamma |\vec{u}| \hat{\mathbf{n}} = C_\gamma |\vec{u}| \frac{\nabla \gamma}{|\nabla \gamma|},$$

$$\mathbf{u}_{R\beta} = C_\beta |\vec{u}| \hat{\mathbf{n}} = C_\beta |\vec{u}| \frac{\nabla \beta}{|\nabla \beta|},$$

The mixture density and viscosity (ρ_m, μ_m) can be computed based on the linear dependence on the distribution of φ, λ, γ and β as:

$$\rho_m = \varphi \rho_1 + \lambda \rho_2 + \gamma \rho_3 + \beta \rho_4 \quad (21)$$

$$\mu_m = \varphi \mu_1 + \lambda \mu_2 + \gamma \mu_3 + \beta \mu_4 \quad (22)$$

3. Numerical methodology

The system of governing Partial Differential Equations (PDE) is solved on a fixed regular Cartesian mesh (i.e. with spacing $\Delta x = \Delta y$) using a Control-Volume method based on the staggered grid system where scalar fields including pressure, viscosity and density are defined

at the cell centers while vector quantities (i.e. velocity components) are stored at the cell faces [61]. The classical second-order central difference scheme is adopted for the treatment of the diffusion terms in Navier-Stokes equations while a novel third-order accurate monotone scheme based on the TVD-NVD concept is first proposed and then utilized for the discretization of the convection terms in momentum, and transport equations. The rigorous derivation of the newly developed third-order bounded advection scheme will be further elaborated upon later (see also Fig. 2). Furthermore, in order to circumvent the problem of pressure-velocity coupling and to eliminate the spurious pressure/velocity fluctuation from the physical discontinuity in the multiphase flows with moving interfaces, a novel semi-iterative pressure-based algorithm is also developed through the combination of the classical SIMPLEC and PISO algorithms (labelled hereafter as CPISO). A more detailed discussion of the proposed coupled CPISO algorithm is presented in Appendix A. The transient terms of the governing equations are discretized implicitly using the classical first order backward-Euler scheme. Finally, for the accurate and efficient imposition of the surface tension force, the second-order accurate piecewise-linear interface reconstruction technique (PLIC-ELVIRA) pioneered by Pilliod et al. [35] is adopted to determine the interface curvature and, therefore, surface tension force. The subroutine related to the PLIC-ELVIRA coded in FORTRAN language is also provided as a supplementary material.

4. A novel third-order bounded advection scheme

Motivated by works of Leonard [37], Choi et al. [45] and Zijlema [69], a novel third-order oscillation-free bounded advection scheme is constructed here by combination of the Total Variational Diminishing and Normalized Variable Diagram constraints (TVD-NVD) for the treatment of the convection terms in Navier-Stokes and transport equations, aiming to circumvent the problem associated with the advection of a step profile (i.e. unphysical undershoots or overshoots) in the Eulerian framework. As sketched in Fig. 2 and listed in Table 1, there exists a one-to-one map between Sweby and NV diagrams [42–44]. The shaded regions highlighted with grey color in both Sweby and NV diagrams convey the TVD area which is bounded by two well-known Minmod and Superbee linear schemes [70]. This suggests that any

Table 1
The linear and non-linear convection schemes defined in the Sweby and NV diagrams.

Scheme	Normalized function in Sweby diagram	Normalized function in NV diagram
1 st order Upwind	$\psi(r) = 0$	$K_f = \Phi_c$
2 nd order Upwind	$\psi(r) = r$	$K_f = \frac{3\Phi_c}{2}$
Quick	$\psi(r) = \frac{r}{4} + \frac{3}{4}$	$K_f = \frac{3\Phi_c}{4} + \frac{3}{8}$
Central	$\psi(r) = 1$	$K_f = \frac{\Phi_c}{2} + \frac{1}{2}$
Van Leer	$\psi(r) = \frac{ r + r}{1 + r}$	$K_f = -\Phi_c^2 + 2\Phi_c$
Minmod	$\psi(r) = \begin{cases} \frac{ r + r}{2} & r \leq 1 \\ 1 & r > 1 \end{cases}$	$\begin{cases} \frac{3}{2}\Phi_c & 0 \leq \Phi_c \leq 0.5 \\ \frac{1}{2}\Phi_c + \frac{1}{2} & 0.5 < \Phi_c \leq 1.0 \\ \Phi_c & 0.5 < \Phi_c - 0.5 \\ 2\Phi_c & 0 \leq \Phi_c \leq \frac{1}{3} \\ \frac{1}{2}\Phi_c + \frac{1}{2} & \frac{1}{3} < \Phi_c \leq \frac{1}{2} \end{cases}$
Superbee	$\psi(r) = \begin{cases} r + r & r \leq 0.5 \\ 1 & 0.5 < r \leq 1 \\ r & 1 < r \leq 2 \\ 2 & r > 2 \end{cases}$	$\begin{cases} \frac{3}{2}\Phi_c & \frac{1}{2} < \Phi_c \leq \frac{2}{3} \\ 1 & \frac{2}{3} < \Phi_c \leq 1 \\ \Phi_c & 0.5 < \Phi_c - 0.5 \\ -\Phi_c^3 - \frac{1}{2}\Phi_c^2 + 2\Phi_c & 0 \leq \Phi_c \leq 0.5 \\ K_f = \begin{cases} -\Phi_c^3 + \frac{3}{2}\Phi_c^2 + \frac{1}{2} & 0.5 < \Phi_c \leq 1.0 \\ \Phi_c & 0.5 < \Phi_c - 0.5 \end{cases} \end{cases}$
Present work	$\psi(r) = \begin{cases} \frac{(r + r) \times (-r^2 + 3r + 2)}{2(1+r)^2} & r \leq 1 \\ \frac{2r^2 + r + 1}{(1+r)^2} & r > 1 \end{cases}$	

smooth curves which lie outside these upper and lower boundaries cannot necessarily preserve monotonicity and are prone to undesirable numerical fluctuations so-called “wiggles” especially in the vicinity of steep gradients of a quantity. To ensure and maintain the monotonic convergence property of the high-order scheme, the following necessary and sufficient criteria formulated by Sweby [39], Leonard [37], Zijlema [69], Gaskell et al. [36] and Alves et al. [41] are utilized:

- To reach the TVD properties, the monotone scheme must be within the asymptotic limits of the Minmod and Superbee schemes (shaded zone) and passes through the points (0,0) and (1,1) in NV diagram,
- To achieve the second-order of accuracy, the monotone scheme must be nonlinear or piecewise linear and passes through the point (0.5, 0.75) in NV diagram,
- To achieve the third-order of accuracy, the monotone scheme must pass through the point (0.5, 0.75) with a slope of 0.75 in NV diagram,
- To satisfy the “smoothness condition”, the monotone scheme must be smooth and has a continuous derivative especially within the shaded region,

By taking the above criteria into consideration, the following piecewise non-linear function can be derived:

$$K_f = \begin{cases} -\Phi_c^3 - \frac{1}{2}\Phi_c^2 + 2\Phi_c & 0 \leq \Phi_c \leq 0.5 \\ -\Phi_c^3 + \frac{3}{2}\Phi_c^2 + \frac{1}{2} & 0.5 < \Phi_c \leq 1.0 \\ \Phi_c & 0.5 < |\Phi_c - 0.5| \end{cases} \quad (23)$$

It is evident from Fig. 2 that, the newly constructed piecewise polynomial function is confined in the shaded area (TVD region) and passes through the points $K_f(0) = 0$ and $K_f(1) = 1$ which ensures boundedness (monotonicity) of the solution while offering the first-order of accuracy which is similar to that observed in classical Upwind scheme ($K_f = \Phi_c$). In addition, similar to the Van Leer bounded advection scheme ($K_f = -\Phi_c^2 + 2\Phi_c$) [71,72], the proposed function passes through the point $K_f(0.5) = 0.75$ which confirms that the model can successfully meet the consistency requirement for second-order accuracy. Moreover, it is not difficult to show that the slope of the piecewise function ($dK_f/d\Phi_c|_{\Phi_c=0.5} = 3/4$) at the intersection point (0.5, 0.75) is the same as that of the standard QUICK scheme ($K_f =$

tangent line. More precisely, it is evident that, the first derivative of each sub-function in Eq. (23) (i.e. $K_{f1} = -\Phi_c^3 - \Phi_c^2/2 + 2\Phi_c$ and $K_{f2} = -\Phi_c^3 + 3\Phi_c^2/2 + 1/2$) at a point (0.5, 0.75) is identical ($dK_{f1}/d\Phi_c|_{\Phi_c=0.5} = dK_{f2}/d\Phi_c|_{\Phi_c=0.5} = 3/4$) which in turn satisfies the “smoothness condition” within the shaded region. The effects of this crucial criterion on the stability of the high-order bounded differencing schemes were systematically examined by Alves et al. [41] and Gao et al. [73] who numerically showed that, the sudden alteration in the slope of advection scheme within the shaded region may results in non-physical velocity fluctuation in close proximity of physical discontinuities especially in the complex three-dimensional turbulent flow calculations. Before proceeding further, it is important to note that in Eq. (23), the normalized variable $\Phi_F = (\phi_F - \phi_U)/(\phi_D - \phi_U)$ represents the ratio of upstream gradient to downstream gradient as defined by Leonard [37]. To shed more light upon the underlying NVD scheme and demonstrate how to implement it in Cartesian framework, the two-dimensional convection-diffusion equation without pressure gradients (∇p) and transient terms ($\partial\rho\phi/\partial t$) are discretized here as an illustration [74]:

$$\frac{d}{dx}(\rho u\phi) + \frac{d}{dy}(\rho v\phi) = \frac{d}{dx}\left[\eta \frac{d\phi}{dx}\right] + \frac{d}{dy}\left[\eta \frac{d\phi}{dy}\right] \quad (24)$$

In the above equation, the term ϕ stands for the general specific property which can be temperature (T), velocity (u, v) or other scalar/vector quantities in the governing equations. By integrating Eq. (24) over the control volume surrounding point P (see also Fig. 2) and implementing the Gauss's divergence theorem in conjunction with the second-order central differencing scheme for diffusion term, the following discretized equation can be derived [61]:

$$F_e\phi_e - F_w\phi_w + F_n\phi_n - F_s\phi_s = D_e(\phi_E - \phi_P) - D_w(\phi_P - \phi_W) + D_n(\phi_N - \phi_P) - D_s(\phi_P - \phi_S) \quad (25)$$

where $F_i = (\rho u)_i \Delta A_i$ with $\Delta A_i = \Delta x = \Delta y$ and $D_i = \eta_i \Delta y / \Delta x = \eta_i \Delta x / \Delta y$ denotes the convection and diffusive flux terms cross the cell boundaries, respectively. By taking into account the direction of the flow ($\mathbf{u}^+ > 0$ or $\mathbf{u}^- < 0$), the values of the property ϕ across the cell faces (ϕ_e , ϕ_w , ϕ_n and ϕ_s) can be estimated as follows:

For the positive flow direction ($\mathbf{u}^+ > 0$)

$$\begin{cases} \frac{\phi_e - \phi_w}{\phi_E - \phi_W} = K_f(\Phi_{c,e}^+), & \phi_e = \phi_w + K_f(\Phi_{c,e}^+) \times (\phi_E - \phi_W), & \Phi_{c,e}^+ = (\phi_P - \phi_W)/(\phi_E - \phi_W) \\ \frac{\phi_w - \phi_{WW}}{\phi_P - \phi_{WW}} = K_f(\Phi_{c,w}^+), & \phi_w = \phi_{WW} + K_f(\Phi_{c,w}^+) \times (\phi_P - \phi_{WW}), & \Phi_{c,w}^+ = (\phi_W - \phi_{WW})/(\phi_P - \phi_{WW}) \\ \frac{\phi_n - \phi_s}{\phi_N - \phi_S} = K_f(\Phi_{c,n}^+), & \phi_n = \phi_s + K_f(\Phi_{c,n}^+) \times (\phi_N - \phi_S), & \Phi_{c,n}^+ = (\phi_P - \phi_S)/(\phi_N - \phi_S) \\ \frac{\phi_s - \phi_{SS}}{\phi_P - \phi_{SS}} = K_f(\Phi_{c,s}^+), & \phi_s = \phi_{SS} + K_f(\Phi_{c,s}^+) \times (\phi_P - \phi_{SS}), & \Phi_{c,s}^+ = (\phi_S - \phi_{SS})/(\phi_P - \phi_{SS}) \end{cases} \quad (26)$$

$3\Phi_c/4 + 3/8$) which in turn fulfills the desired third-order accuracy. Analogous to CICSAM [46], SHARP [37] and SOUCUP [45] schemes, the proposed function switches smoothly between its sub-functions and approaches the critical point of (0.5, 0.75) with the same slope of the

By adding and subtracting the variables ϕ_p , ϕ_w , ϕ_p and ϕ_s in/from the right hand side of the above equation, the unnormalized form of Eq. (26) can be rewritten as:

For the positive flow direction ($\mathbf{u}^+ > 0$)

$$\begin{cases} \phi_e = \phi_p + (\phi_w - \phi_p) + K_f(\Phi_{c,e}^+) \times (\phi_e - \phi_w), & \Phi_{c,e}^+ = (\phi_p - \phi_w)/(\phi_e - \phi_w) \\ \phi_w = \phi_w + (\phi_{ww} - \phi_w) + K_f(\Phi_{c,w}^+) \times (\phi_p - \phi_{ww}), & \Phi_{c,w}^+ = (\phi_w - \phi_{ww})/(\phi_p - \phi_{ww}) \\ \phi_n = \phi_p + (\phi_s - \phi_p) + K_f(\Phi_{c,n}^+) \times (\phi_n - \phi_s), & \Phi_{c,n}^+ = (\phi_p - \phi_s)/(\phi_n - \phi_s) \\ \phi_s = \phi_s + (\phi_{ss} - \phi_s) + K_f(\Phi_{c,s}^+) \times (\phi_p - \phi_{ss}), & \Phi_{c,s}^+ = (\phi_s - \phi_{ss})/(\phi_p - \phi_{ss}) \end{cases} \quad (27)$$

likewise, in the case of negative flow direction, the values of the property ϕ across the cell faces (ϕ_e , ϕ_w , ϕ_n and ϕ_s) can be expressed as:

For the negative flow direction ($\mathbf{u}^- < 0$)

coefficient (a_p) is always positive and can effectively fulfill the needs for conservativeness and transportiveness as highlighted by Versteeg et al. [61]. The allocation to the source term (S_u) of the part of the discretization that contains negative coefficients is known as “*deferred correction*” (DC) which can be expressed as:

$$\begin{cases} \frac{\phi_e - \phi_{EE}}{\phi_p - \phi_{EE}} = K_f(\Phi_{c,e}^-), & \phi_e = \phi_{EE} + K_f(\Phi_{c,e}^-) \times (\phi_p - \phi_{EE}), & \Phi_{c,e}^- = (\phi_e - \phi_{EE})/(\phi_p - \phi_{EE}) \\ \frac{\phi_w - \phi_E}{\phi_w - \phi_E} = K_f(\Phi_{c,w}^-), & \phi_w = \phi_E + K_f(\Phi_{c,w}^-) \times (\phi_w - \phi_E), & \Phi_{c,w}^- = (\phi_p - \phi_E)/(\phi_w - \phi_E) \\ \frac{\phi_n - \phi_{NN}}{\phi_p - \phi_{NN}} = K_f(\Phi_{c,n}^-), & \phi_n = \phi_{NN} + K_f(\Phi_{c,n}^-) \times (\phi_p - \phi_{NN}), & \Phi_{c,n}^- = (\phi_N - \phi_{NN})/(\phi_p - \phi_{NN}) \\ \frac{\phi_s - \phi_N}{\phi_s - \phi_N} = K_f(\Phi_{c,s}^-), & \phi_s = \phi_N + K_f(\Phi_{c,s}^-) \times (\phi_s - \phi_N), & \Phi_{c,s}^- = (\phi_p - \phi_N)/(\phi_s - \phi_N) \end{cases} \quad (28)$$

By adding and subtracting the variables ϕ_E , ϕ_p , ϕ_N and ϕ_s from the right hand side of the above equation, the unnormalized form of Eq. (28) can be rewritten as:

For the negative flow direction ($\mathbf{u}^- < 0$)

$$\begin{cases} \phi_e = \phi_E + (\phi_{EE} - \phi_E) + K_f(\Phi_{c,e}^-) \times (\phi_p - \phi_{EE}), & \Phi_{c,e}^- = (\phi_E - \phi_{EE})/(\phi_p - \phi_{EE}) \\ \phi_w = \phi_p + (\phi_E - \phi_p) + K_f(\Phi_{c,w}^-) \times (\phi_w - \phi_E), & \Phi_{c,w}^- = (\phi_p - \phi_E)/(\phi_w - \phi_E) \\ \phi_n = \phi_N + (\phi_{NN} - \phi_N) + K_f(\Phi_{c,n}^-) \times (\phi_p - \phi_{NN}), & \Phi_{c,n}^- = (\phi_N - \phi_{NN})/(\phi_p - \phi_{NN}) \\ \phi_s = \phi_p + (\phi_N - \phi_p) + K_f(\Phi_{c,s}^-) \times (\phi_s - \phi_N), & \Phi_{c,s}^- = (\phi_p - \phi_N)/(\phi_s - \phi_N) \end{cases} \quad (29)$$

However, since the high-resolution differencing scheme (e.g. QUICK, SMART, SHARP, etc) are vulnerable to numerical instability owing to the emergence of negative main coefficients, Eqs. (27) and (29) in the NVD concept can be generalized and reformulated by incorporating the notation of Upwind scheme as follows:

$$\begin{aligned} a_p \phi_p &= a_w \phi_w + a_E \phi_E + a_s \phi_s + a_N \phi_N + S_u \\ a_w &= D_w + \max(F_w, 0) \\ a_E &= D_e + \max(-F_e, 0) \\ a_s &= D_s + \max(F_s, 0) \\ a_N &= D_n + \max(-F_n, 0) \\ a_p &= a_w + a_E + a_s + a_N + (F_e - F_w) + (F_n - F_s) \end{aligned} \quad (30)$$

One of the main advantages of the above equation is that, the main

$$\begin{aligned} S_u &= -\gamma_e F_e \left[(\phi_w - \phi_p) + K_f(\Phi_{c,e}^+) \times (\phi_E - \phi_w) \right] \\ &\quad + \gamma_w F_w \left[(\phi_{ww} - \phi_w) + K_f(\Phi_{c,w}^+) \times (\phi_p - \phi_{ww}) \right] \\ &\quad - \gamma_n F_n \left[(\phi_s - \phi_p) + K_f(\Phi_{c,n}^+) \times (\phi_N - \phi_s) \right] \\ &\quad + \gamma_s F_s \left[(\phi_{ss} - \phi_s) + K_f(\Phi_{c,s}^+) \times (\phi_p - \phi_{ss}) \right] \\ &\quad - F_e (1 - \gamma_e) \left[(\phi_{EE} - \phi_E) + K_f(\Phi_{c,e}^-) \times (\phi_p - \phi_{EE}) \right] \\ &\quad + F_w (1 - \gamma_w) \left[(\phi_E - \phi_p) + K_f(\Phi_{c,w}^-) \times (\phi_w - \phi_E) \right] \\ &\quad - F_n (1 - \gamma_n) \left[(\phi_{NN} - \phi_N) + K_f(\Phi_{c,n}^-) \times (\phi_p - \phi_{NN}) \right] \\ &\quad + F_s (1 - \gamma_s) \left[(\phi_N - \phi_p) + K_f(\Phi_{c,s}^-) \times (\phi_s - \phi_N) \right] \end{aligned} \quad (31)$$

In the above source term, γ_i is the constant parameter which depends on the direction of the flow defined as:

$$\begin{aligned}\gamma_e &= 1 \text{ if } F_e > 0, & \gamma_e &= 0 \text{ if } F_e < 0 \\ \gamma_w &= 1 \text{ if } F_w > 0, & \gamma_w &= 0 \text{ if } F_w < 0 \\ \gamma_n &= 1 \text{ if } F_n > 0, & \gamma_n &= 0 \text{ if } F_n < 0 \\ \gamma_s &= 1 \text{ if } F_s > 0, & \gamma_s &= 0 \text{ if } F_s < 0\end{aligned}\quad (32)$$

Before ending this subsection, it is relevant to mention that, in order to avoid or minimize excessive use of "IF" in computer programming of the proposed scheme and to prevent any possible singularity in denominator of the subdomains (i.e. $0 \leq \Phi_c \leq 0.5, 0.5 < \Phi_c \leq 1.0$ and $0.5 < |\Phi_c - 0.5|$) in Eq. (23), special treatment should be applied to each sub-domain of piecewise polynomial function. To address this issue, one can multiply the numerator and denominator of gradient ratio (Φ_c) with the value of its denominator (e.g. $\Phi_c = A/B = A \times B/B^2$). Take as an illustration, the normalized variable of $\Phi_{c,e}^+$ on the East cell face for the positive flow direction can be written as:

$$\Phi_{c,e}^+ = \frac{(\phi_p - \phi_w)}{(\phi_E - \phi_w)} = \frac{(\phi_p - \phi_w)}{(\phi_E - \phi_w)} \times \frac{(\phi_E - \phi_w)}{(\phi_E - \phi_w)} = \frac{(\phi_p - \phi_w) \times (\phi_E - \phi_w)}{(\phi_E - \phi_w)^2} \quad (33)$$

By applying the above procedure on the Eq. (23), one can obtain:

For sub-domain ($0 \leq \Phi_{c,e}^+ \leq \frac{1}{2}$)

$$\begin{aligned}0 &\leq \frac{(\phi_p - \phi_w) \times (\phi_E - \phi_w)}{(\phi_E - \phi_w)^2} \leq \frac{1}{2} \rightarrow 0 \leq (\phi_p - \phi_w) \times (\phi_E - \phi_w) \\ &\leq \frac{(\phi_E - \phi_w)^2}{2}\end{aligned}$$

For sub-domain ($\frac{1}{2} < \Phi_{c,e}^+ \leq 1$)

$$\begin{aligned}\frac{1}{2} &\leq \frac{(\phi_p - \phi_w) \times (\phi_E - \phi_w)}{(\phi_E - \phi_w)^2} \leq 1 \rightarrow \frac{(\phi_E - \phi_w)}{2} \\ &\leq (\phi_p - \phi_w) \times (\phi_E - \phi_w) \leq (\phi_E - \phi_w)^2\end{aligned}\quad (34)$$

For sub-domain $\frac{1}{2} < |\Phi_{c,e}^+ - \frac{1}{2}|$

$$\begin{aligned}\frac{1}{2} &< \left| \frac{(\phi_p - \phi_w) \times (\phi_E - \phi_w)}{(\phi_E - \phi_w)^2} - \frac{1}{2} \right| \rightarrow (\phi_E - \phi_w)^2 \\ &< |2 \times (\phi_p - \phi_w) \times (\phi_E - \phi_w) - (\phi_E - \phi_w)^2|\end{aligned}$$

Note that, the similar procedure should be applied to other three faces of computational grid (i.e. $\Phi_{c,e}^-, \Phi_{c,w}^+, \Phi_{c,n}^+$ and $\Phi_{c,s}^+$) by considering the related neighboring grid points and direction of the flow. Finally, as stated earlier, Gao et al. [44], Chourushi [42] and Lima et al. [43] mathematically demonstrated that, there is a one-to-one correlation between Sweby and NV diagrams such that by implementing the following relationship:

$$K_f = \Phi_c + \frac{1}{2}\psi(r) \times (1 - \Phi_c), \quad r = \frac{\Phi_c}{1 - \Phi_c} \quad (35)$$

the corresponding flux-limiter function ($\psi(r)$) in Sweby diagram can be derived. Take as an illustration, by substituting Eq. (23) into Eq. (35), the proposed model can be converted into piecewise non-linear function in the context of Sweby diagram:

$$\psi(r) = \begin{cases} \frac{(|r| + r) \times (-r^2 + 3r + 2)}{2(1+r)^2} & r \leq 1 \\ \frac{2r^2 + r + 1}{(1+r)^2} & r > 1 \end{cases} \quad (36)$$

For more details related to the discretization process of governing equations using the Sweby concept, the interested reader is referred to our previous work [63].

5. Validation

The feasibility and reliability of the newly proposed high resolution TVD-NVD bounded advection scheme together with hybrid PISO-SIMPLEC algorithm (CPISO) in handling multi-fluid flows with arbitrarily shaped interfaces and large topological changes (i.e. merging, deforming, breaking, rupturing, and folding) are systematically verified against six different two-dimensional benchmark cases. As schematically shown in Fig. 1, the first canonical test case is the well-known dam failure problem (case 1) where due to the occurrence of wave overturning, the angle between the interface and direction of motion becomes equal to 45°, making it a suitable candidate to account for the effects of flow-to-grid skewness. The second challenging problem is a dam break flow with a stationary obstacle (case 2) where due to the emergence of the oblique ascending jet and high level of air-water interaction, the phenomena so-called interface dispersing/wrinkling and noisy pressure field are likely to appear within the computational domain, thereby enabling us to further examine the performance of ELVIRA and CPISO models in reconstructing interfacial and suppressing spurious pressure oscillation in close proximity of the contact discontinuities. The third example under consideration are classical three-fluid rising bubble (case 3) where due to the presence of three distinct fluids, an extra advection equation for the colour function will be coupled to the Navier-Stokes equations. The fourth, fifth and sixth challenging problems are classical two-fluid (cases 4 & 5) and three-fluid Rayleigh-Taylor Instability (case 6) which can provide a sufficient difficulty to challenge the performance of the proposed TVD-NVD bounded advection scheme.

With the help of these challenging benchmark cases, the capability of the enhanced VOF model in dealing with multiphase flows with large deformation and twisting will be demonstrated. The obtained results are presented in forms of volume fraction and pressure contours alongside the time history of the interface positions.

5.1. Dam-break flow over a dry bed (Case 1)

In order to testify the accuracy and stability of the improved VOF model in predicting the mechanics of plunging wave impact, the classical dam break flow advancing in a straight channel is reproduced in this sub-section. A schematic of the experimental prototype is depicted in Fig. 1. This problem was originally carried out by Martin et al. [75] and then was numerically analyzed by Ling et al. [76] and Sheu et al. [77] in the framework of Eulerian description using coupled VOF-Level-Set model. As it can be observed, the spatial domain consists of a rectangular flume with dimensions of $L = 1$ m and $D = 0.25$ m where the volume of water ($\rho_{Water} = 1000 \text{ kg/m}^3, \mu_{Water} = 0.001 \text{ kg/ms}$) with initial depth and length of $W = H = 0.2$ m is installed on the left half of the enclosure. The rest of the computational domain is filled with air ($\rho_{Air} = 1.0 \text{ kg/m}^3, \mu_{Air} = 184 \times 10^{-7} \text{ kg/ms}$) as a secondary phase. The surface tension coefficient and gravity acceleration are set equal to $\sigma = 0.071 \text{ Kgs}^{-2}$ and $g = 9.81 \text{ m/s}^2$, respectively. No-slip velocity boundary condition is applied on all solid walls ($\mathbf{u} = 0$) and the calculation is performed on 500×125 grid stencils ($\Delta x = \Delta y = 0.002 \text{ m}$). To monitor pressure variations, three virtual pressure sensors are deployed on the right (h_{Ri}) wall of the channel while water level height is measured at the dam site ($l_1 = 0.003 \text{ m}$). The predicted results in forms of pressure and volume fraction contours are portrayed in Fig. 3 at different non-dimensional time instants ($T = t\sqrt{g/H}$). The predicted results in Fig. 3 reveal that, after opening the virtual barrier ($0 \leq T \leq 3.138$), the stored water collapses and propagates horizontally until the water front reaches the right boundary at around $T = 2.90$ with maximum velocity of $V_{max} = 2\sqrt{gH}$ where the first impact pressure ($P_{max1} = 2.205$) takes place [78]. Since the downstream end wall is rigid and impermeable, the wave front starts to change its direction and deviates upward, producing an ascending jet along the vertical wall. In such circumstances, due to

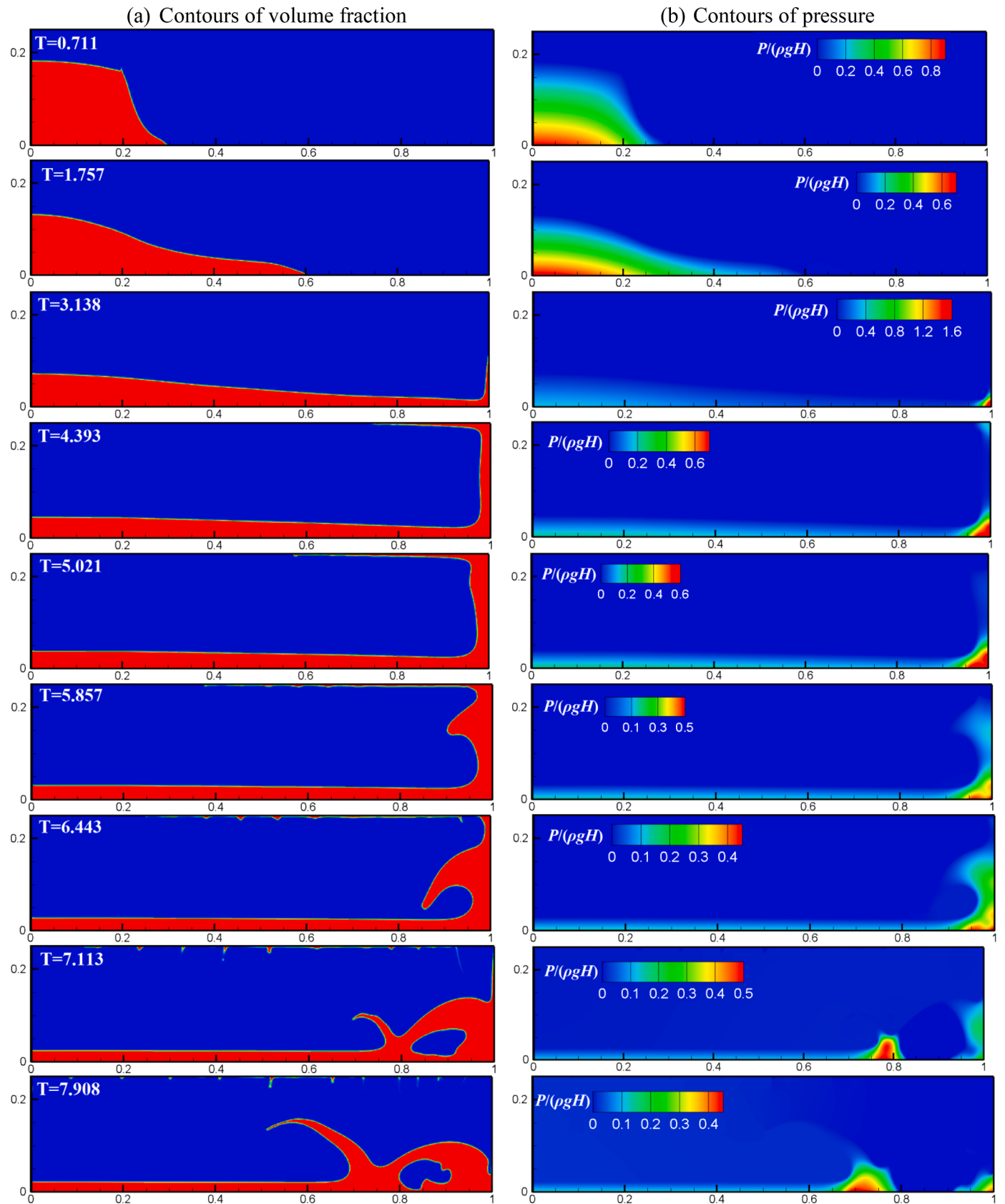


Fig. 3. Time evolution of dam-break flow over a dry bed (case 1) in forms of the volume-fraction and pressure fields computed in the present work at different time instants. ($T = t\sqrt{g/H}$).

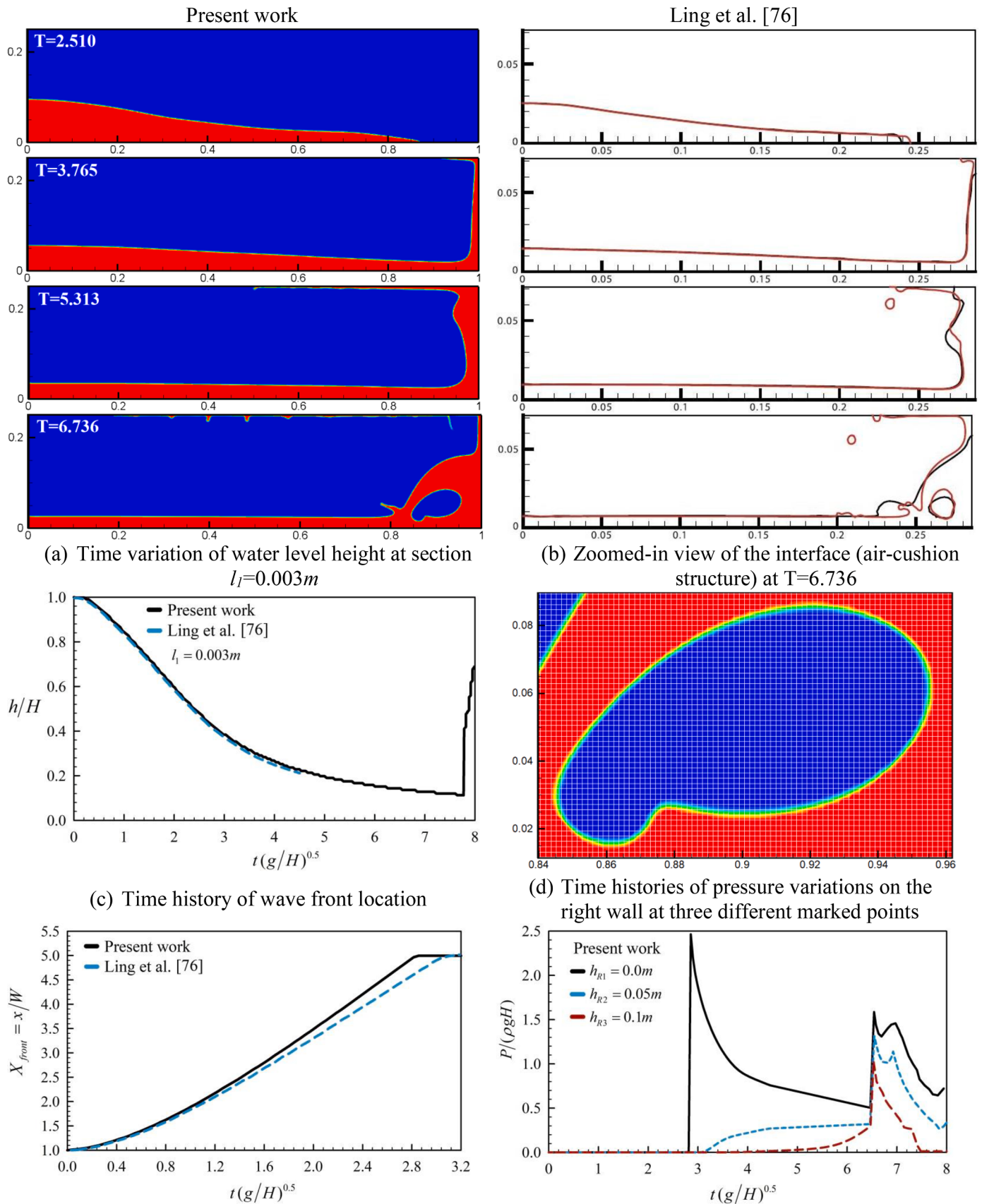


Fig. 4. Qualitative and quantitative comparison of the obtained results with numerical data of Ling et al. [76] in case 1.

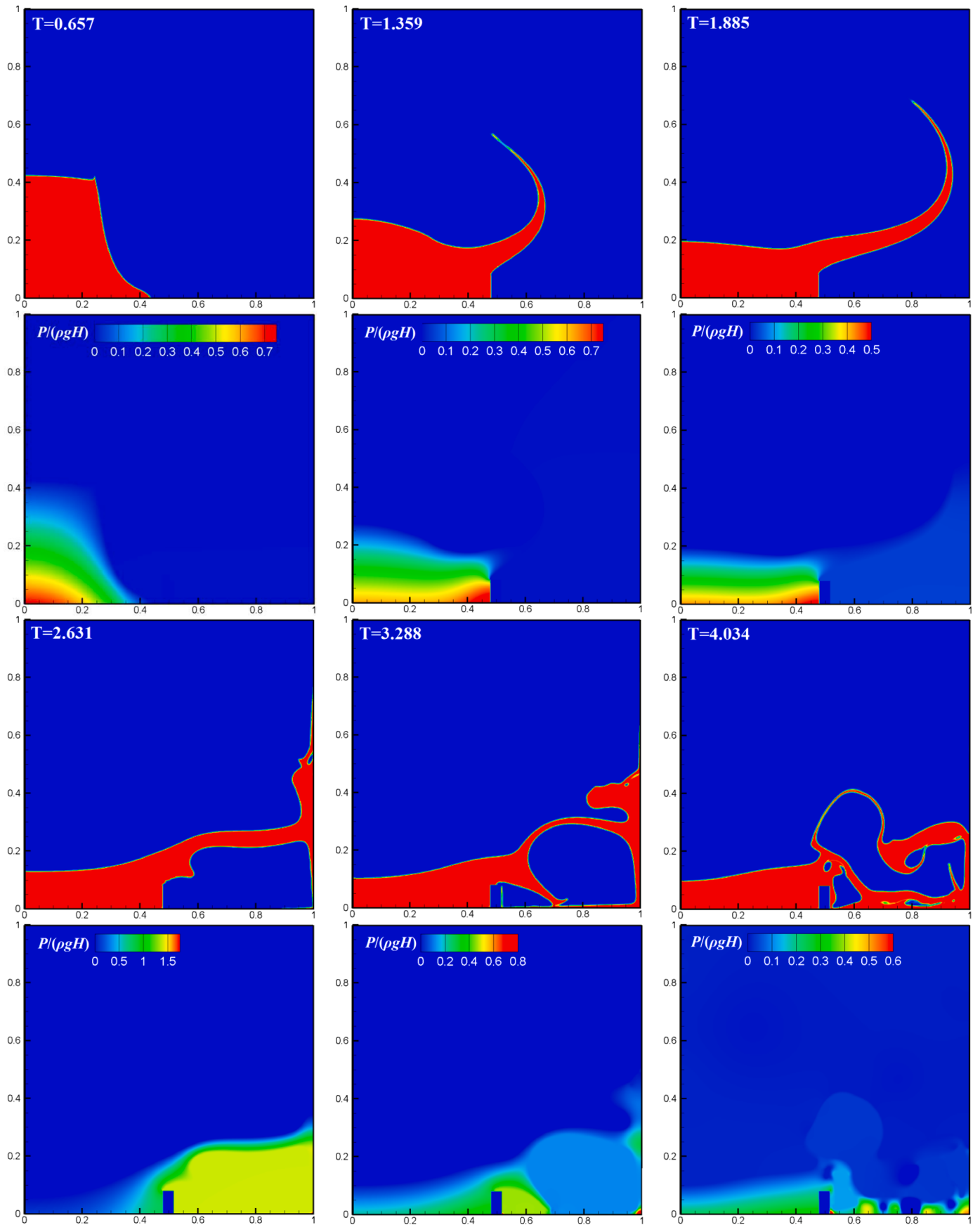


Fig. 5. Time evolution of dam-break flow with a stationary obstacle (case 2) in forms of the volume-fraction and pressure fields computed in the present work at different time instants. ($T = t\sqrt{g/H}$).

the abrupt change in the direction of the wave front, the movement of the leading edge is distracted and a considerable amount of kinetic energy is irreversibly converted into shock structure. This hydrodynamic change manifests itself through the enhancement in pressure distribution and attenuation in the mean velocity magnitude. Note that, a small portion of kinetic energy is also dissipated viscously to establish the macro-recirculating zone on the bottom-right corner of the enclosure where the shock pressure is progressively evolved into quasi-hydrostatic

pressure distribution. This mechanism in the literature is known as a fluid trapping phenomenon in which a clockwise rotating eddy is developed in the shock zone and keeps growing in size as the rising jet spreads upward. Before proceeding further, it is important to stress that, as documented by Colagrossi et al. [79], the maximum run up point of the rising jet along the downstream wall typically exceeds twice of initial water level at the dam site ($Y_{\max, \text{jet}} = V_{\max}^2 / 2g = 2H$) which is theoretically consistent with the maximum celerity of the dam-break wave

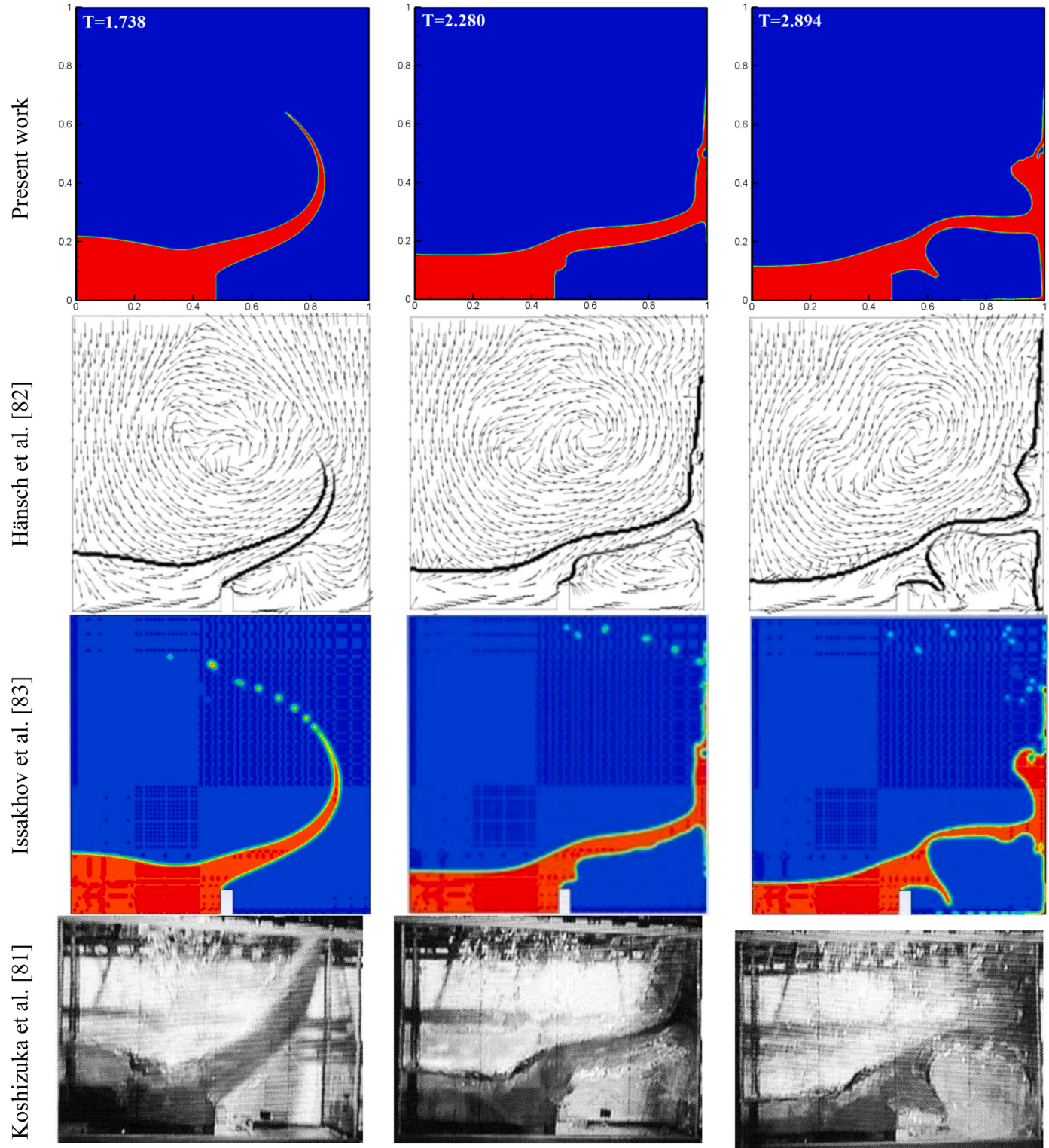


Fig. 6. Qualitative comparison of the obtained results with numerical data of Hänsch et al. [82], Issakhov et al. [83] and Koshizuka et al. [81] for case 2.

front. However, in this example due to the small distance between top and bottom walls ($D = 0.25m < 2H$), the up-running wave eventually impinges on the top horizontal boundary, leading to the development of second shock pressure and recirculating clockwise vortex on that area (see snapshots of the free-surface evolution during the time period of $(3.138 < T \leq 4.393)$). Later, owing to the restoring action of gravity force, the kinetic energy of the ascending jet declines and consequently the upwelling surge wave decelerates and begins to retreat toward the lower portion of the enclosure. However, due to the obstructing effects of oncoming dam break flow, the stagnation point is formed in the immediate vicinity of the right wall approximately at the height and time of $Y \approx 0.2m$ and $T = 5.021$, respectively which is the strong indication for the longitudinal velocity reduction and transverse velocity augmentation. It is constantly perceived that this physical model ultimately causes the fluid to detach from the solid wall and overturn backward in form of a plunging wave ($5.021 < T \leq 5.854$). As time goes on ($5.854 < T \leq 6.443$), the acceleration of fluid motion is invigorated and consequently the appearance of plunging breaker gets more prominent. As anticipated, due to the instability in wave profile, the plunging jet eventually hits the underlying wetted bed, leading to the occurrence of the third shock pressure ($T = 6.611, P_{\max 2} = 1.58$) and large air roller within the enclosure. It can be seen from Fig. 3 that, the impact of the breaking jet on water surface of the incoming flow induces a new surge which rebounds from the bulk motion and travels obliquely toward the upstream with moderate celerity during the period of $T = 6.443$ to 7.908 . Note that, aided by the action of impinging motion, the second plunging breaker becomes noticeable and some secondary vortices are created at the intersection of the impact zone and underlying main body. This

assertion is in accordance with experimental and numerical findings of Li et al. [80] who pointed out that, at the onset of rebounding process, three distinct clockwise/counter-clockwise (CW/CCW) vortices are likely to emerge in close proximity of air-cavity structure induced by a plunging solitary wave namely: (1) a CCW eddy which is trapped within the "tube" induced by the curling wave, (2) a CCW eddy which is established by the reflected/rebounded jet as it collides the wetted deck, and (3) a CW eddy which is appeared between the aforementioned vortices and starts to rotate in the opposite direction.

Qualitative and quantitative comparisons of obtained results with numerical data of Ling et al. [76] in Fig. 4 vividly reveal that all hydrodynamic features and morphological characteristics of dam failure flow in terms of collapsing, surging, plunging and rebounding events are well predicted by the improved VOF model. More precisely, it is evident that, the pressure distribution in vicinity of the physical discontinuity is totally smooth without any unphysical noises which in turn confirms the robustness and capability of the hybrid PISO-SIMPLEC algorithm in handling multiphase flows with large topological changes and impact/slaming events. Furthermore, the close-up view of the air-cushion structure in Fig. 3 demonstrates that, the thickness of the interface is well controlled and restricted into the maximum 2-3 grid spaces which clearly prove the accuracy of the proposed TVD-NVD bounded scheme in suppressing the detrimental effects of false-diffusion errors and preserving the sharpness of the interface. Based on the above description, one can conclude that, the existence of small discrepancy between two outcomes may be attributed to the implementation of low resolution differencing schemes used by Ling et al. [76] for discretization of the governing equations.

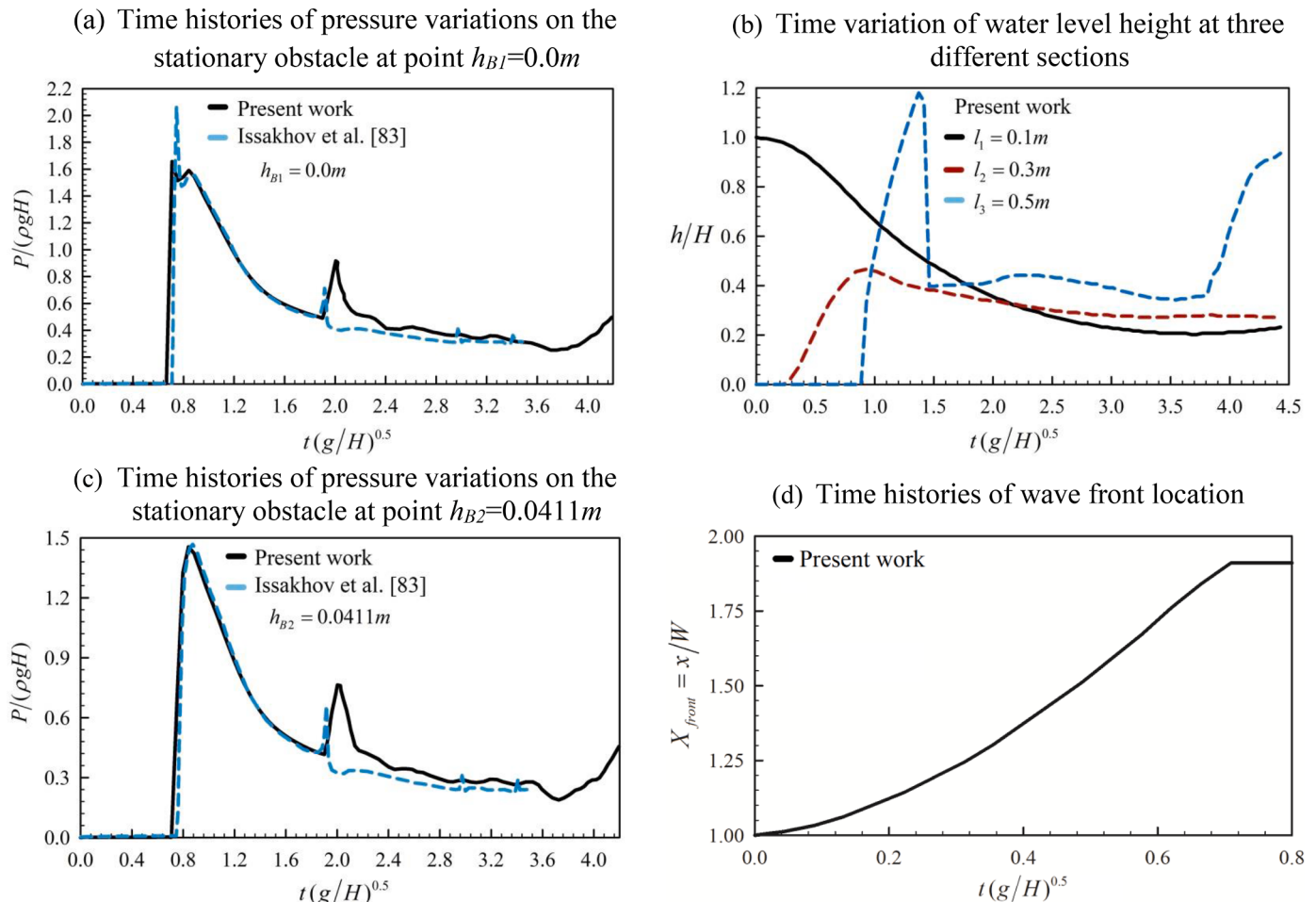


Fig. 7. Quantitative comparison of the obtained results with numerical data of Issakhov et al. [83] in case 2.

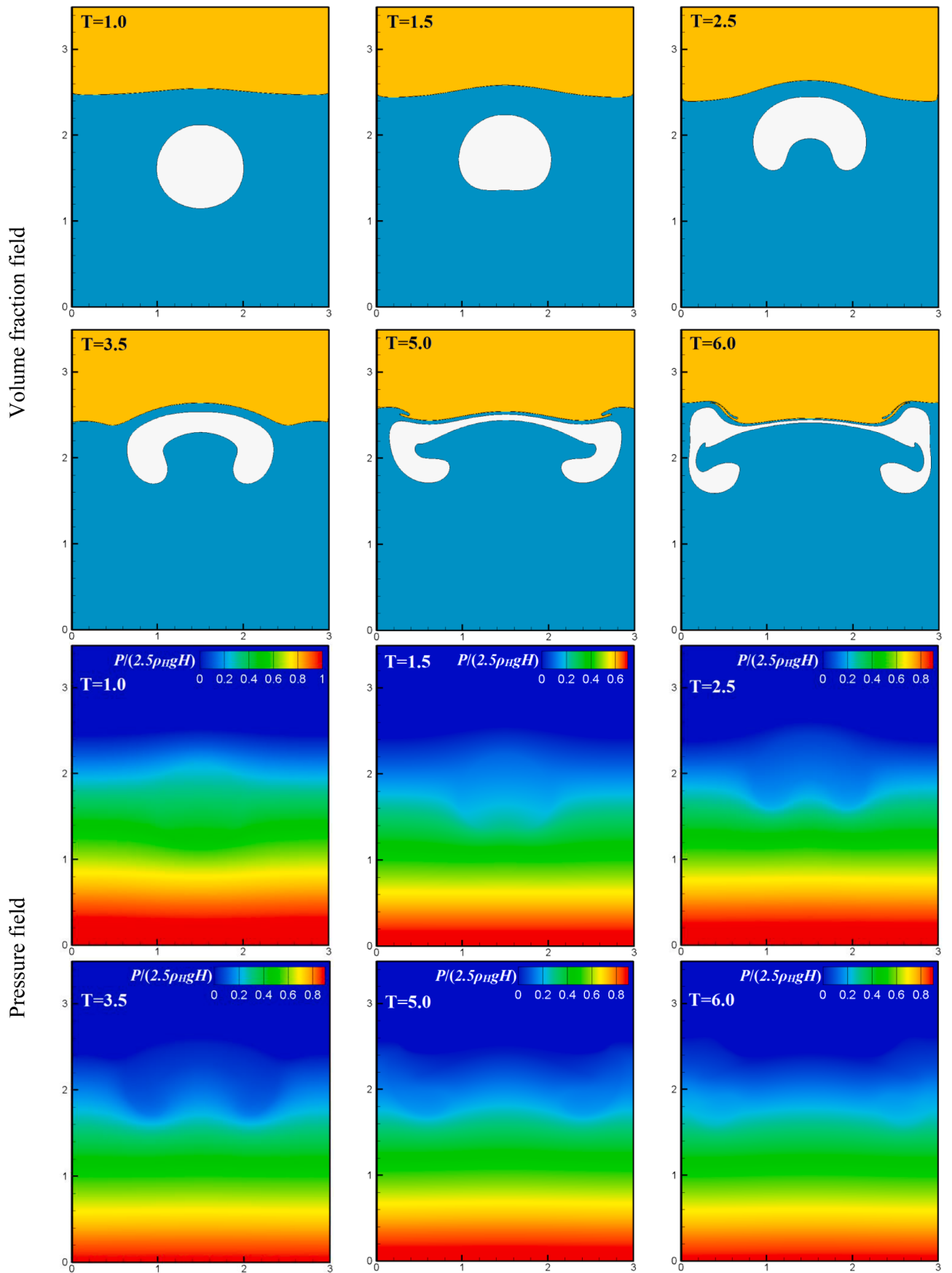


Fig. 8. Time evolution of three-fluid rising bubble (case 3) in terms of the volume-fraction and pressure fields computed in the present work at different time instants.

5.2. Dam-break flow with a stationary obstacle (Case 2)

The second test case considers a sudden interaction between the baffle and the dam flow. This violent free-surface flow was originally introduced by Koshizuka et al. [81] and then was numerically reproduced by Hänsch et al. [82], Issakhov et al. [83] and Peng et al. [84]. The initial laboratory prototype experiment with corresponded nominal parameters is depicted in Fig. 1. The configuration is square in shape ($L = D = 1\text{ m}$) with a rectangular cross section. A rigid obstacle with length and height of $B_1 = 0.0411\text{ m}$ and $B_2 = 0.0822\text{ m}$ is deployed at the middle of the bottom wall ($x = 0.5\text{ m}$), dividing the capacity into two separate compartments as upstream and downstream. The upstream area is initially occupied with rectangular still water ($H = 0.5\text{ m}, W = 0.25\text{ m}$) while the downstream is dry and occupied by air. The physical properties of working fluids are same as ones used in the previous test case. As sketched in Fig. 1, three vertical wave probes at positions $l_1 = 0.1\text{ m}, l_2 = 0.3\text{ m}, l_3 = 0.5\text{ m}$ together with two pressure sensors installed on the left side of the obstacle ($h_{B1} = 0.0\text{ m}, h_{B2} = 0.0411\text{ m}$) are utilized to monitor the variations of the water surface elevation and pressure time histories during the solid-fluid interaction. No-slip velocity boundary condition is applied on all solid walls ($\mathbf{u} = 0$) and the predicted results in terms of volume fraction and pressure contours at some selected non-dimensional time instants ($T = t\sqrt{g/H}$) are portrayed in Fig. 5. It is evident that, once the virtual gate is removed, the water column releases suddenly and flows horizontally until it touches the obstacle at $T = 0.708$. At this moment, the main flow undergoes remarkable deflection in which the velocities decline rapidly and the pressure rockets up, resulting in the development of the first shock wave (or peak pressure) at the bottom-left corner of the barrier ($P_{\max 1} = 1.656$). However, similar to the previous test case, with the elapse of time ($1.359 \leq T \leq 1.885$), the pressure solution gradually recovers to the quasi-hydrostatic one and consequently a clockwise recirculating eddy is form in the impact zone. Meanwhile, the resultant stress wave jumps over the obstacle and drifts upward in an oblique manner until it encounters opposite wall where the second shock pressure occurs. The instantaneous sudden rise in the pressure time histories ($T = 2.017, P_{\max 2} = 0.936$) in Fig. 7 suggests that the reflected rarefaction and compression waves have been transmitted into the liquid phase and are captured by sensors 1 and 2 deployed on the left side of the obstacle. This slant jet, however, exerts additional impact force on the front vertical wall of the reservoir and initiates the second run-down/run-up cycle. By this mechanism, a reverse overturning solitary wave (plunging breaker) is generated above the impact point and starts to grow in the middle of the domain as the water sheet is projected downward due to gravity ($2.631 \leq T \leq 3.288$). A close inspection of the numerical results in Fig. 5 also shows that during this period of time, the small gas structure on the crest of plunging breaker has vanished and the secondary water tongue near the boundary of the obstacle is impinged onto the bottom wall, leading to the formation of the small closed loop in that area. Similar morphological alterations were also reported by Hänsch et al. [82] who investigated the identical canonical test case using Eulerian two-phase model. It can be seen from Fig. 5 that, as the overturning jet in the upper half of the enclosure propagates laterally toward the water sheet ($3.288 < T \leq 4.034$), the air-water interface undergoes intense filamentation and ultimately bursts/raptures at the free surface. It is evident that during the stretching of the fluid interface, the frontal edge of the well-developed plunging jet hits the tail of the filament, thereby forming a third air pocket structure inside the breaking loop. Note that, outside the overturning region, the interface movement is mainly governed by the effects of the air-entrainment and violent splashing events together with “*plunging vortex*” which results in a significant air-water mixing as observed by Lin et al. [85]. The sequence of the wave profiles in Fig. 6 shows that the predicted results from the current work are in good qualitative agreement with those obtained by Koshizuka et al. [81], Hänsch et al. [82] and Issakhov et al. [83]. More precisely, it is evident

from Figs. 5 to 7 that, the moments of first and second impact loads are well captured by the proposed model and transient evolution of the interfacial layer in terms of interface deforming, merging and bursting has been accurately converged to the benchmark solutions without spurious numerical dissipation/diffusion, certifying the capability of the enhanced VOF model in handling complex arbitrarily shaped interfaces with large fragmentation and coalescence. Finally, for the sake of completeness, the time histories of wave front location before impinging onto the obstacle and water level elevations at three marked section are provided in Fig. 7 as additional information which have not been reported in the published literature.

5.3. Three-fluid rising bubble (Case 3)

As a further validation of the proposed enhancements, the dynamic evolution of three-fluid bubble rising in a partially filled container is analyzed in this subsection. This challenging test case was originally introduced by Pan et al. [86] and was then investigated numerically by Sheu et al. [77], Ming et al. [87], Li et al. [88] and Zhao et al. [89] using VOF, Level-set and SPH models. As schematically portrayed in Fig. 1, the computational model consists of a rectangular cavity with width and height of $3H$ and $3.5H$ where $H = D = 2R = 1.0\text{ m}$ denotes the diameter of the circular bubble. The enclosure is filled with three different immiscible fluids with nominal densities of $\rho_L = 10\text{ kg/m}^3$, $\rho_M = 500\text{ kg/m}^3$ and $\rho_H = 1000\text{ kg/m}^3$ where the subscripts L , M and H are assigned to the lighter, middle and heavier fluids, respectively. The bubble is initially centered at $X_M = 1.5H = 1.5\text{ m}, Y_M = 1.5H = 1.5\text{ m}$ surrounded by the denser fluid with depth of $Y_H = 2.5H = 2.5\text{ m}$. The flow regime is governed by Froude and Reynolds numbers defined as $Fr = u/\sqrt{gH} = 1.0$ and $Re = \rho_H H \sqrt{gH}/\mu_H = 200$ with $u = \sqrt{gH}$ being the reference velocity. Similar to Ref [86], for the sake of convenience, the surface tension effect has not been included in the present problem and the kinematic viscosity of all fluids is chosen to be equal to each other ($\nu_H = \nu_M = \nu_L = 0.01\text{ m}^2/\text{s}$). The simulation is conducted on the uniform grid distribution of 300×350 and no-slip boundary condition is enforced on all rigid walls ($\mathbf{u} = 0$). Note that, since three different fluids are involved in this benchmark test case, Eqs. (4) and (5) are employed to determine the interface position of dense and middle fluids while Eq. (6) ($\varphi + \lambda + \gamma = 1$) are utilized to identify the location of lighter fluid. The physical properties of working fluids are also approximated linearly via Eqs. (9) and (10), respectively. The time sequence of bubble rising as a function of non-dimensional time ($T = t\sqrt{g/D}$) is depicted in Fig. 8. From the flow-visualization results of Fig. 8 it can be observed that, in general, driven by the buoyancy force, the circular bubble ascends upward and starts to push up the interfacial layer between dense (ρ_H) and lighter (ρ_L) fluids. Meanwhile, in order to satisfy the need for the mass conservation law, the heavy fluid descends downward and travels toward the position originally occupied by the rising bubble, leading to the development of two symmetric recirculating eddies within the enclosure. This mechanism, in turn, causes the tails of the bubble to fold inward and consequently the formation of the vortex shedding in the wake of the bubble becomes more prominent. However, since no surface tension is involved, the rolling wave excited by the wake shed causes the bubble to pierce from the bottom and evolve into the shape of horseshoe. Beyond the initial stage, the motion of perforating jet gradually slows down and subsequently the bubble begins to broaden transversely, resulting in the appearance of kidney-shaped structure at around $T = 3.5$. From the spatial anatomy of the interfacial layers, one can conclude that, as the bubble elongates in the x -direction, due to the imposition of the no-slip boundary condition on the vertical walls, two small bumps are developed adjacent to the vertical solid walls and start to transform into plunging jet as time enhances ($3.5 \leq T \leq 5.5$). The growth of the breaking-like motion indicates that the fluids attached to the solid walls are practically frozen and some secondary vortices have been established in those regions.

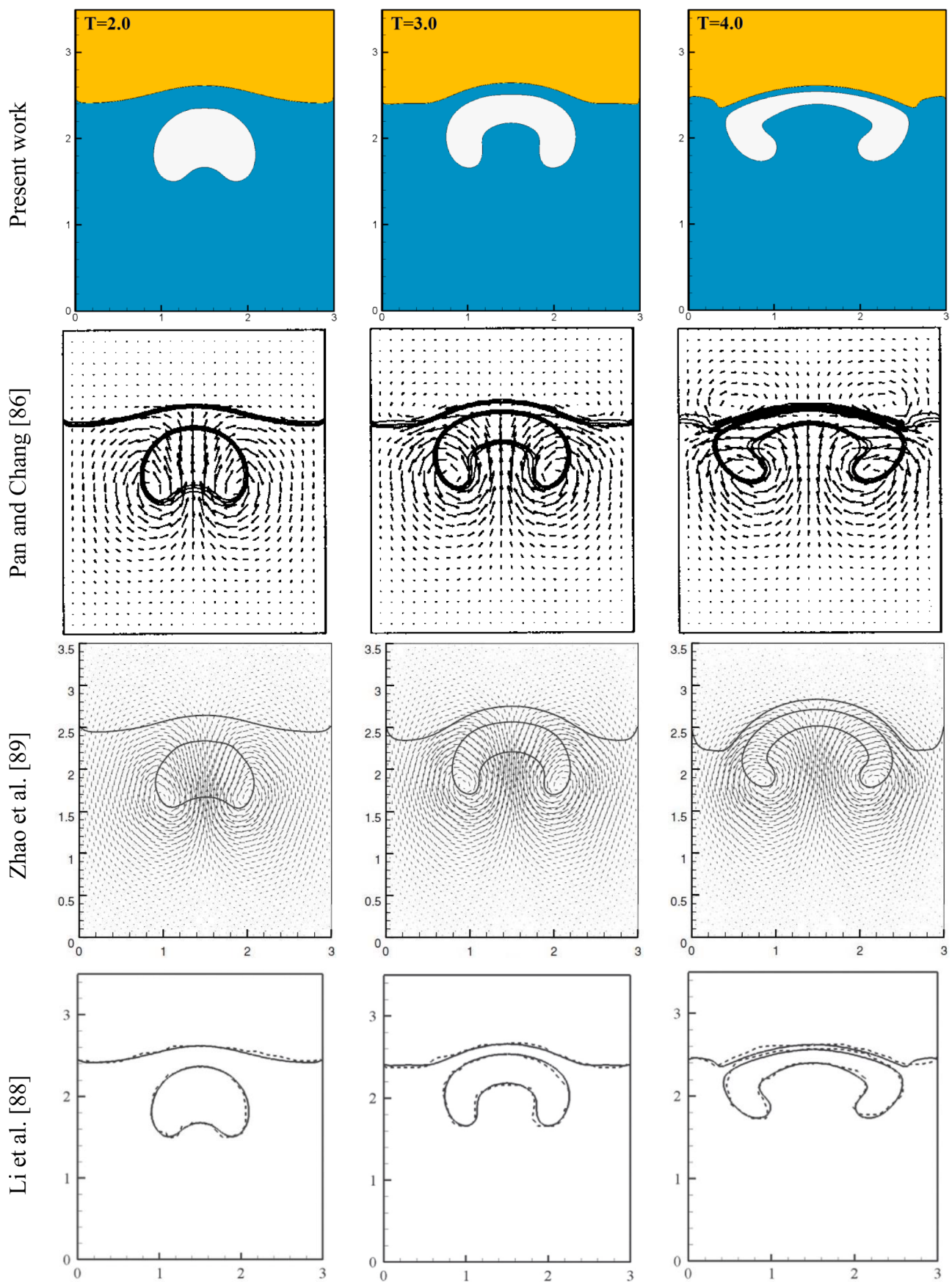
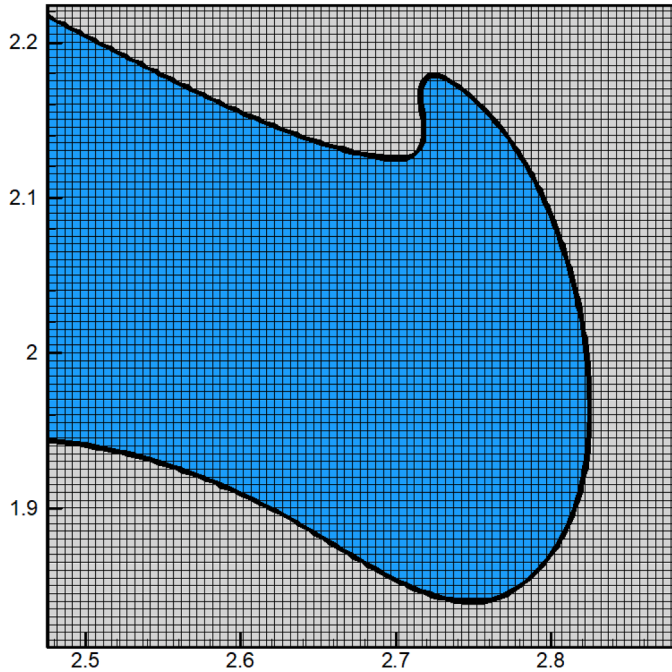


Fig. 9. Qualitative comparison of the obtained results with numerical data of Pan et al. [86], Li et al. [88] and Zhao et al. [89] in case 3.

(a) Zoomed-in view of the bubble interface at $T=6.0$ 

(b) Positions of the interfacial layers

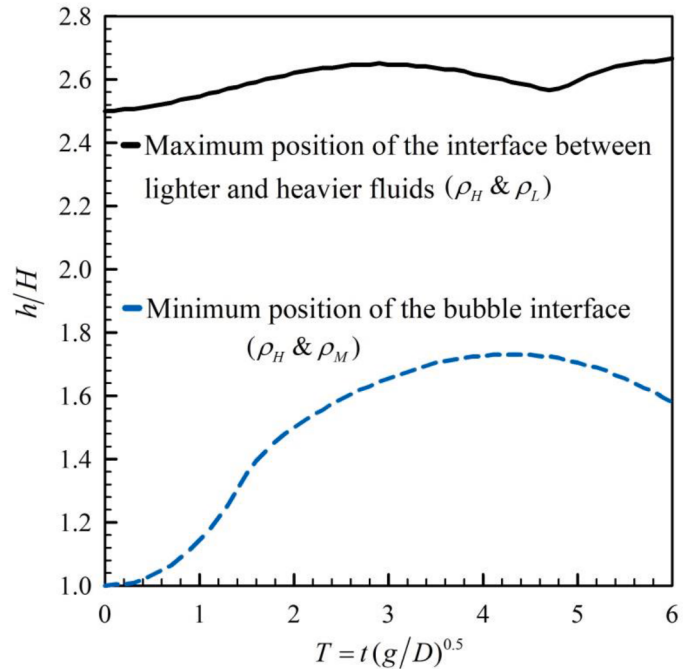


Fig. 10. (a) Zoomed-in view of the bubble interface and (b) the time histories of maximum and minimum positions of the interfaces computed from the present study in case 3.

However, in the last stage due to the relative dominance of shear force versus the buoyancy, the lower surface of the skirted bubble exhibits strong non-linearity which may be attributed to the appearance of the Kelvin-Helmholtz instability. In fact, the existence of high tensile stresses along the shrinking neck of the bubble causes two primary vortices to become unstable and consequently the bubble undergoes substantial twisting/stretching. This flow pattern is consistent with the flattening and filamentation of the bubble interface and its transfiguration into mushroom-like structure.

The obtained results are compared with the corresponding benchmark solution at three different time instants in Fig. 9 and excellent agreement is found between three numerical outcomes. Moreover, the close-up view of the final bubble shape at $T=6.0$ in Fig. 10 shows that, the thickness of the interfacial layers between nominally immiscible liquids take only 2-3 grid spacing which indicates that the false numerical diffusion is immensely alleviated by the proposed bounded advection scheme. Thanks to the noise-free characteristics of the developed pressure-based solver, the corresponding pressure variations are quite smooth in space domain which in turn affirms the robustness and efficiency of the hybrid PISO-SIMPLEC algorithm in preventing the induction of excessive spurious velocities across the interface. Finally, the minimum and maximum positions of the interfacial layers between working fluids are provided in Fig. 10 as supplementary data which have been reported in the previous studies.

5.4. Two-fluid Rayleigh-Taylor Instability (Cases 4 and 5)

In this subsection the problems of two-fluid Rayleigh-Taylor Instability (2D RTI) proposed by Cummins et al. [90] and Shadloo et al. [91] are reproduced using the enhanced VOF model. As highlighted before, the mixing of two immiscible fluids under the influence of gravity force can provide sufficient level of difficulty to challenge the interface-capturing methods [92–94]. As schematically shown in Fig. 1, the simulation in case 4 is conducted in the rectangular domain of $[H, 2H]$ where $H = 1.0\text{ m}$ denotes the width of the enclosure. Similar to previous works of Pahar et al. [95], Garoosi et al. [96] and Rezavand

et al. [97], the calculation is carried out on 250×500 grid resolution and the effects of surface tension force is ignored. To initiate the instability, two incompressible viscous fluids with nominal densities of $\rho_L = 1.0\text{ kg/m}^3$ and $\rho_H = 1.8\text{ kg/m}^3$ are sequentially installed in the lower and upper portions of the container. The fluid flow is governed by Atwood and Reynolds numbers given by $At = (\rho_H - \rho_L)/(\rho_H + \rho_L) = 2/7$ and $Re = \rho_H H \sqrt{gH}/\mu_H = 420$ where $\mu_H = 0.018\text{ Kg/ms}$ is the viscosity of the dense fluid. The kinematic viscosity of both fluids is chosen to be equal to each other ($\nu_H = \nu_L = 0.01\text{ m}^2/\text{s}$). The fluids are initially separated by an interface located at $y = 1.0 - 0.15 \times \sin(2\pi x)$. No-slip boundary condition is imposed on both horizontal and vertical walls ($\mathbf{u} = 0$) and the predicted results in form of volume fraction contour at various non-dimensional time ($T = t\sqrt{g/H}$) are depicted in Fig. 11. It can be seen that, due to the existence of the density gradient between two adjacent fluids, the heavy fluid falls down in vicinity of the left wall while the lighter fluid moves upward in proximity of the right wall under the action of the buoyancy force, forming two counter-rotating vortices within the computational domain. As time elapses, due to the small density differences, the interface becomes unstable to the Kelvin-Helmholtz Instability (KHI) and consequently the appearance of the mushroom-like structure gets more prominent. It is evident that by this mechanism, the symmetry of the mixed region is gradually vanished which indicates that the growth rate of RTI is mainly driven by the shear stresses. As time goes on, the intensity of the vortices increases which causes the interface to roll-up/roll-down into the bubble-spoke structure. However, due to the appearance of the nonlinearities and the imposition of the lower no-through flow boundary on the horizontal wall, the velocity of the fluid flow decreases, giving rise to a much stronger contraction and distortion of the descending/ascending spike-bubble structure. Coming to the comparison of the global characteristics of the flow between the Eulerian and Lagrangian approaches in Figs. 11 and 12, a good agreement can be found between four numerical solutions. It can be observed that, the bubble-spoke structure is accurately reproduced by the proposed VOF model and the thickness of the moving interface is successfully restricted into maximum 2-3 grid spacing (see

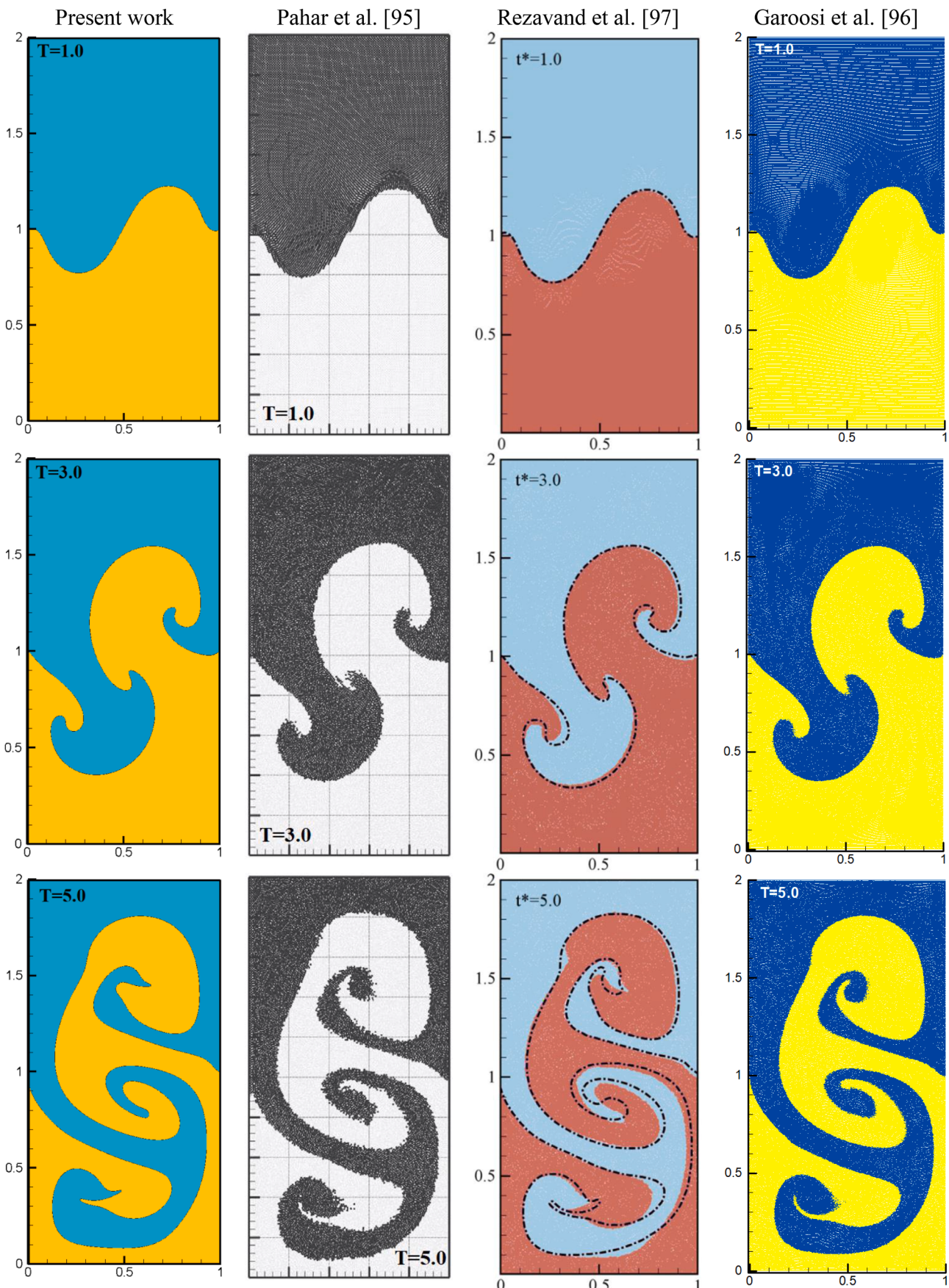


Fig. 11. Qualitative comparison of the obtained results with numerical data of Pahar et al. [95], Rezavand et al. [97] and Garoosi et al. [96] in case 4 (two-fluid Rayleigh-Taylor Instability).

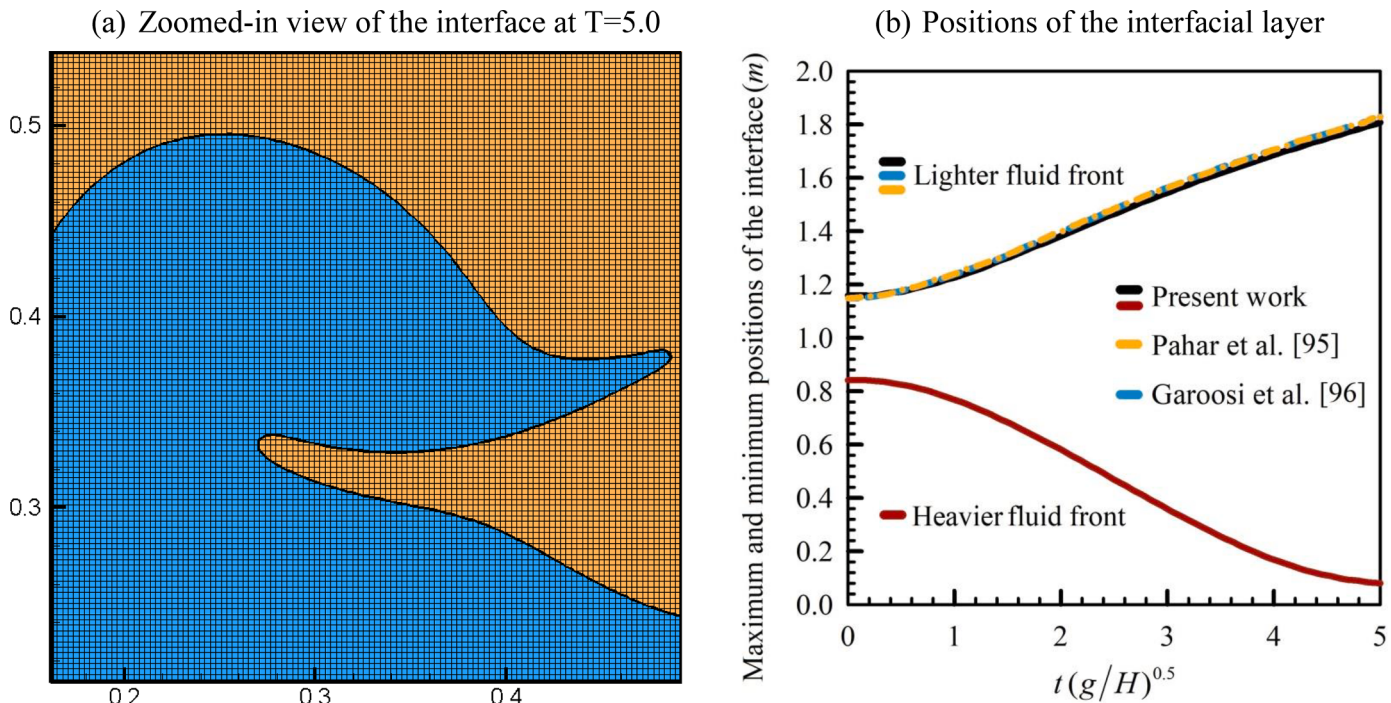


Fig. 12. (a) Zoomed-in view of the interface and (b) quantitative comparison of the obtained results with numerical data of Pahar et al. [95], Rezavand et al. [97] and Garoosi et al. [96] in case 4.

enlarged view of the interface at $T=5.0$ in Fig. 12). Furthermore, Fig. 12 (b) shows that, the time history of the maximum position of the interface computed by the proposed VOF model is in excellent agreement with those obtained by SPH [95] and MPS [96] models.

In the same context, the transient development of mixing of two immiscible incompressible fluids with different densities subjected to an external acceleration introduced by Shadloo et al. [91] in Lagrangian description (i.e. SPH) is examined here as a second challenging 2D Rayleigh-Taylor Instability problem. As schematically portrayed in Fig. 1, the calculation in case 5 is performed in the rectangular domain of $[H, 4H]$ where $H = 1.0\text{ m}$ represents the width of the container. The initial position of the perturbed interface is set as $y = 2.0 + 0.05 \times \cos(2\pi x)$. The no-slip boundary conditions are prescribed for velocity at the top and bottom walls whereas the periodic boundary conditions are enforced on the vertical walls. To initiate the instability, the heavy fluid with density and viscosity of $\rho_H = 2.0\text{ kg/m}^3$ and $\mu_H = 0.028\text{ Kg/ms}$ is placed above the lighter fluid with physical properties of $\rho_L = 1.0\text{ kg/m}^3$ and $\mu_L = 0.014\text{ Kg/ms}$, giving rise to the Atwood and Reynolds numbers equal to $At = (\rho_H - \rho_L)/(\rho_H + \rho_L) = 1/3$ and $Re = \rho_H H \sqrt{gH}/\mu_H = 300$, respectively. The calculation is performed on 200×800 grid resolution and the effects of surface tension force are ignored. The comparison of the obtained results with numerical data of Shadloo et al. [91] at different non-dimensional time instants ($T = t\sqrt{g/H}$) is plotted in Fig. 13. It can be seen that, at the early stages of the evolution ($0 \leq T \leq 1.848$) where the linear theory is valid, the heavier fluid penetrates into the lighter one in form of spike while the lighter fluid ascends upward in form of the bubble, leading to the formation of two counter-rotating vortices and a symmetrical spike-bubble structure within the enclosure. However, in the intermediate stage of development ($1.848 < T \leq 3.692$), due to the intensification of the shear velocity, two primary vortices become unstable and consequently the tails of the spike start to roll-up which indicates that the KHI is coming into the picture. This mechanism may explain the anticipated formation of some secondary eddies on the tails of the spike and the onset of the weakly nonlinear stage (or bubble-spike asymmetry), accordingly. Similar observations were also reported by Celani et al. [98] who

discovered that the deviation from the linear theory typically occurs when the perturbation amplitude exceeds $0.1\lambda - 0.4\lambda$ ($\lambda = 1.0\text{ m}$ is the wave length of the perturbed interface ($\lambda \equiv 2\pi/k$)). As the perturbation grows further ($3.692 < T \leq 5.544$), the intensity of the fluid flow increases, thereby causing the bubble-spike structure to transform into the mushroom shaped plume. As the time proceeds ($5.544 < T \leq 7.224$), the role of the KHI becomes more prominent which causes the fluid interface to elongate vertically and fold into very complicated shape. A close inspection of the results in Fig. 13 reveals that, the total displacement of the falling fluid is considerably higher than that of the rising fluid. This observation is in accordance with numerical findings of Talat et al. [99], Luo et al. [100,101] who investigated the RTI phenomenon at different Atwood number ($0.1 \leq At \leq 0.5$) and concluded that at $0.2 \leq At$ the heavy front moves much faster than the lighter one. In the last stages of the development, the rising/falling velocity of plumes decreases, indicating some saturation of bubble/spike growth. When it comes to the comparison of the obtained results with numerical outcomes of Shadloo et al. [91] in Lagrangian framework, the satisfactory agreement can be found between two solutions. However, there exists some small discrepancies between two numerical methods which can be attributed to the existence of some crucial drawbacks associated with Lagrangian particle method (i.e. SPH model) namely: smoothing errors, particle clustering (i.e. tensile instability) and low order-order of accuracy of differencing schemes [102]. More precisely, the results of Agertz et al. [103], Bender et al. [104] and Sun et al. [105] showed that, the classical governing operators defined in the SPH context (i.e. gradient, Laplacian and divergence) cannot accurately resolve multi-level vorticity and are inherently characterized by numerical dissipation/diffusion. These numerical shortcomings in turn can lead to the substantial loss of accuracy and unphysical wake/pressure distributions around the fluid interface. However, the comparison of the obtained results with numerical data of Shadloo et al. [91] in terms of bubble front in Fig. 14 (b) reveals that, the maximum position of the interface is accurately captured by the enhanced VOF model. Finally, the enlarged view of the interface in Fig. 14 (b) vividly confirms that, the proposed VOF model can produce sharp resolution of material discontinuity without introducing excessive smearing.

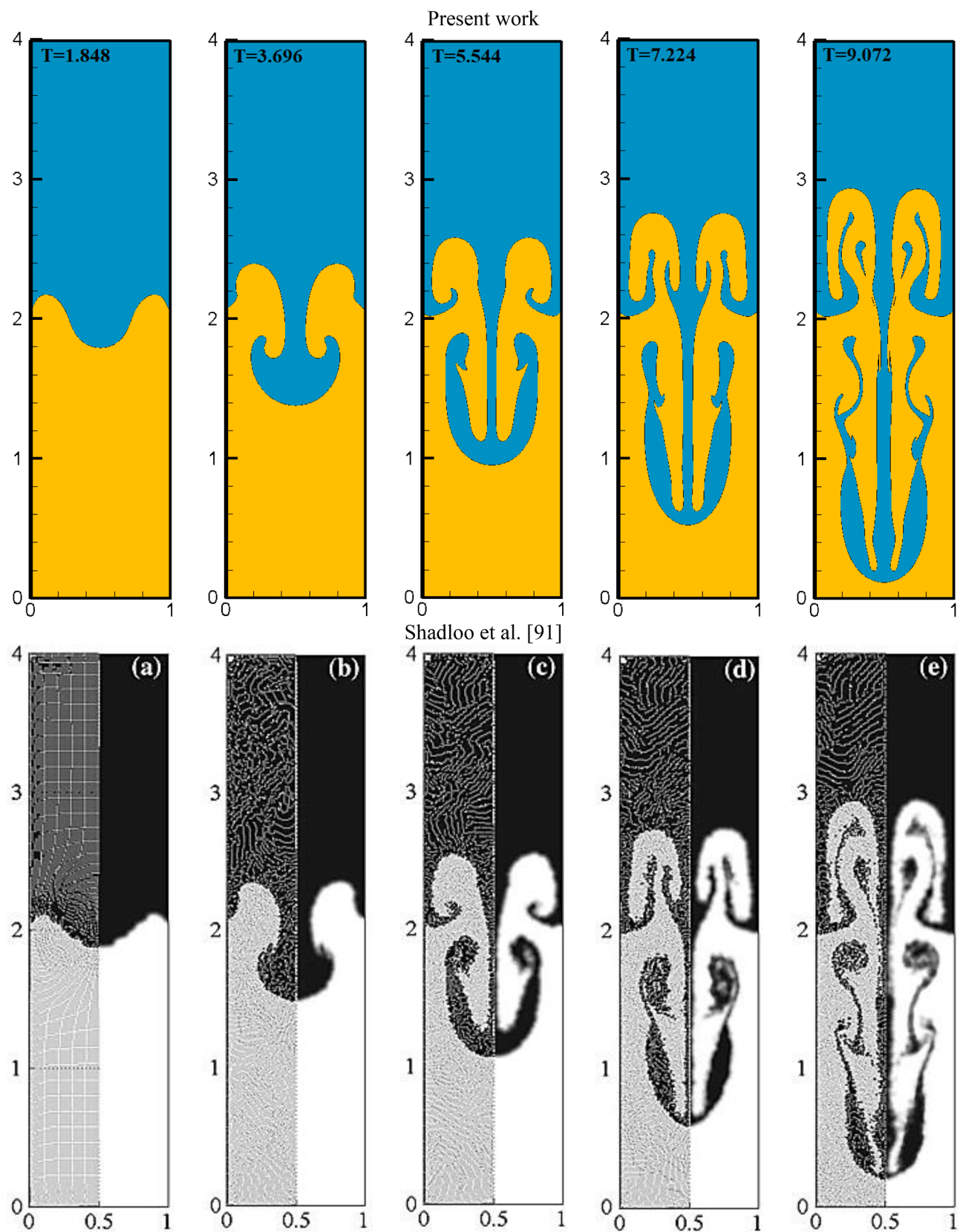


Fig. 13. Qualitative comparison of the obtained results with numerical data of Shadloo et al. [66] in case 5.

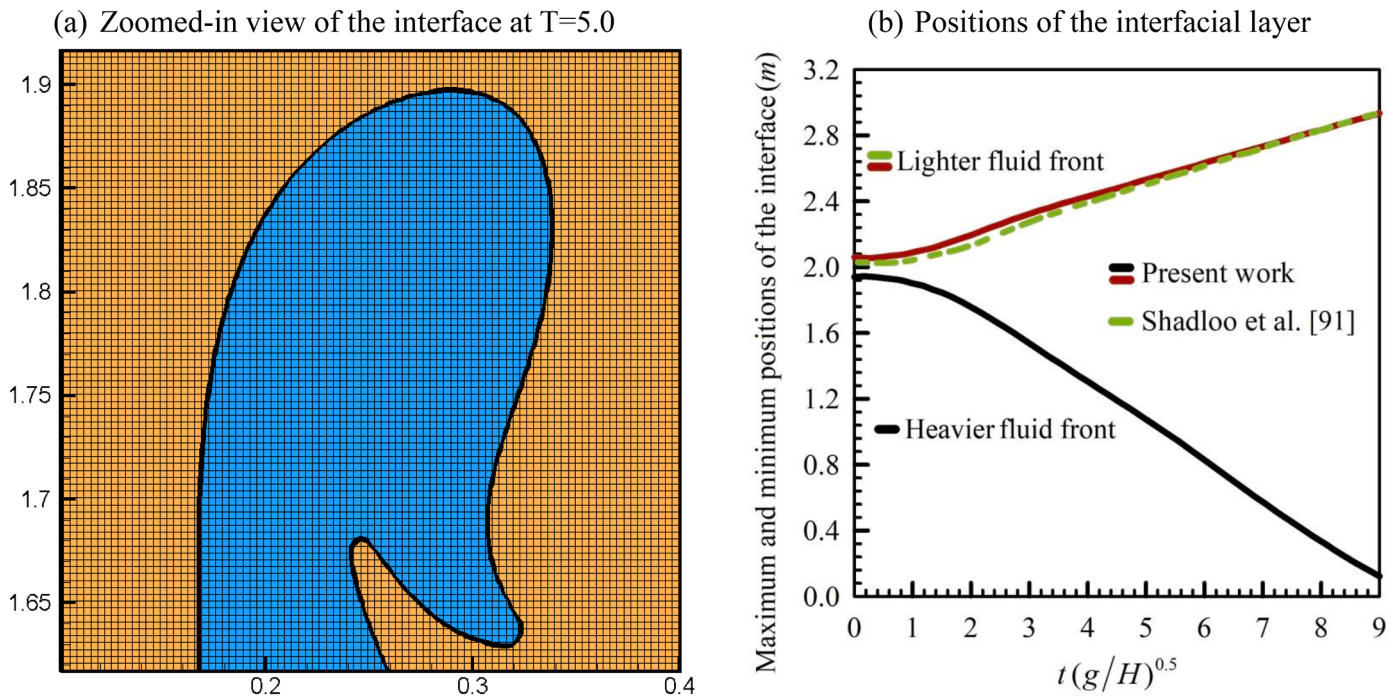


Fig. 14. (a) Zoomed-in view of the interface and (b) quantitative comparison of the obtained results with numerical data of Shadloo et al. [91] in case 5.

5.5. Three-fluid Rayleigh-Taylor Instability (Case 6)

To further affirm the consistency and accuracy of the proposed modifications in maintaining thin filaments, the spatial and temporal evolutions of three-fluid Rayleigh-Taylor Instability (RTI) introduced by Aly [106] is analyzed in this subsection using the improved VOF model. This phenomenon was first computed by means of mesh-free SPH model defined in the context of the Lagrangian description and thus perceived to be difficult to implement on mesh-based Eulerian framework, making it more suitable to challenge the capability of proposed model. As displayed in Fig. 1, the numerical analysis is executed in a square domain ($[1m, 1m]$) where three incompressible viscous fluids with nominal densities of $\rho_L = 2/3 \text{ kg/m}^3$, $\rho_M = 1.0 \text{ kg/m}^3$ and $\rho_H = 3/2 \text{ kg/m}^3$ are sequentially installed in the lower, middle and upper portions of the enclosure. The instability is governed by Atwood and Reynolds numbers given by $A_t = (\rho_H - \rho_L)/(\rho_H + \rho_L) = 5/13$ and $Re = \rho_H H \sqrt{gH}/\mu_H = 8400$ where $H = 1.0 \text{ m}$ and $g = 17.64 \text{ m/s}^2$ are width of the computational domain and gravity acceleration, respectively. The interface between two adjacent fluids are initially perturbed by sinusoidal functions as $y_1 = 0.333 - 0.05 \times \sin(6\pi x)$ and $y_2 = 0.666 - 0.05 \times \sin(6\pi x)$. The governing equations are discretised on uniform mesh elements (450×450) and the effects of surface tension force are not taken into consideration. The kinematic viscosity of all working fluids is equal to each other ($\nu_L = \nu_M = \nu_H = 5 \times 10^{-4} \text{ m}^2/\text{s}$) and no-slip boundary condition is applied on all solid walls ($\mathbf{u} = 0$). The snapshots of the predicted results at different non-dimensional time ($T = t\sqrt{g/H}$) are plotted in Fig. 15. Generally, due to the disturbed interfaces, the hydrodynamic equilibrium between fluids gradually dies out and the instability begins to grow vertically through collapsing the heavy fluid from the upper part of the enclosure and ascending the lighter one from the bottom portion. As instability intensifies, the dense (ρ_H) and light (ρ_L) fluids penetrate further into the middle fluid (ρ_M) and the formation of spike-bubble structures becomes more visible. This stage is accompanied by the rapid conversion of internal energy into kinetic one which manifests itself through the appearance of the small-scale toroidal vortices and inner rolled-up/rolled-down structures along the moving interfaces. It can be seen that, after the concentrated eddies are formed, the flow

pattern deviates slightly from a diagonally symmetric structure and the elongation of the interfaces gets more prominent. In this circumstance, the amplitude and propagation of the spike and bubble increase and consequently the fluid flow becomes unstable to Kelvin-Helmholtz shear Instability (KHI). Note that, as highlighted by Grétar Tryggvason [107], the onset of KHI is responsible for the advection of the secondary “vortex blobs” (or simply the “blobs”) and hence any departure from the symmetry condition. As time progresses, the dense and light fluids continuously intrude into the middle fluid and eventually start to envelop each other. At this stage, the resultant interfacial layers attain very complicated shapes which indicate that the RTI is entered into the non-linear regime.

Coming to the comparison of the volume fraction field in Fig. 15 at $T=2.343$, there is satisfactory agreement of the global characteristics of the RTI evolution between the predicted results and those reported by Aly [106]. However, the small discrepancies between two outcomes may be attributed to the natures of the numerical models used for the calculations. To be more specific, the classical SPH model is typically characterized by two numerical shortcoming namely “tensile instability” and “non-conservative pressure gradient” which can immensely jeopardize the reliability and accuracy of the numerical simulations [108]. In addition to that, the governing operators in the context of the SPH model (i.e. Laplacian and gradient) at their best conditions can reach the second order of accuracy both in time and space whereas the proposed model benefits from third-order of consistency [109]. This assertion is in accordance with numerical findings of Sun et al. [105] who mathematically demonstrated that the problems of “smoothing error” and the “discretization error” can immensely influence the performance and accuracy of the particle based approaches. Finally, similar to the previous test cases, the time histories of the maximum and minimum positions of the lighter and denser fluid are presented in Fig. 15 as additional data which have not been reported in the previous literature.

6. Results and discussion

In the previous part of the study, the versatility and robustness of the proposed modifications in predicting the hydrodynamic details of violent free-surface and multiphase problems were successfully verified

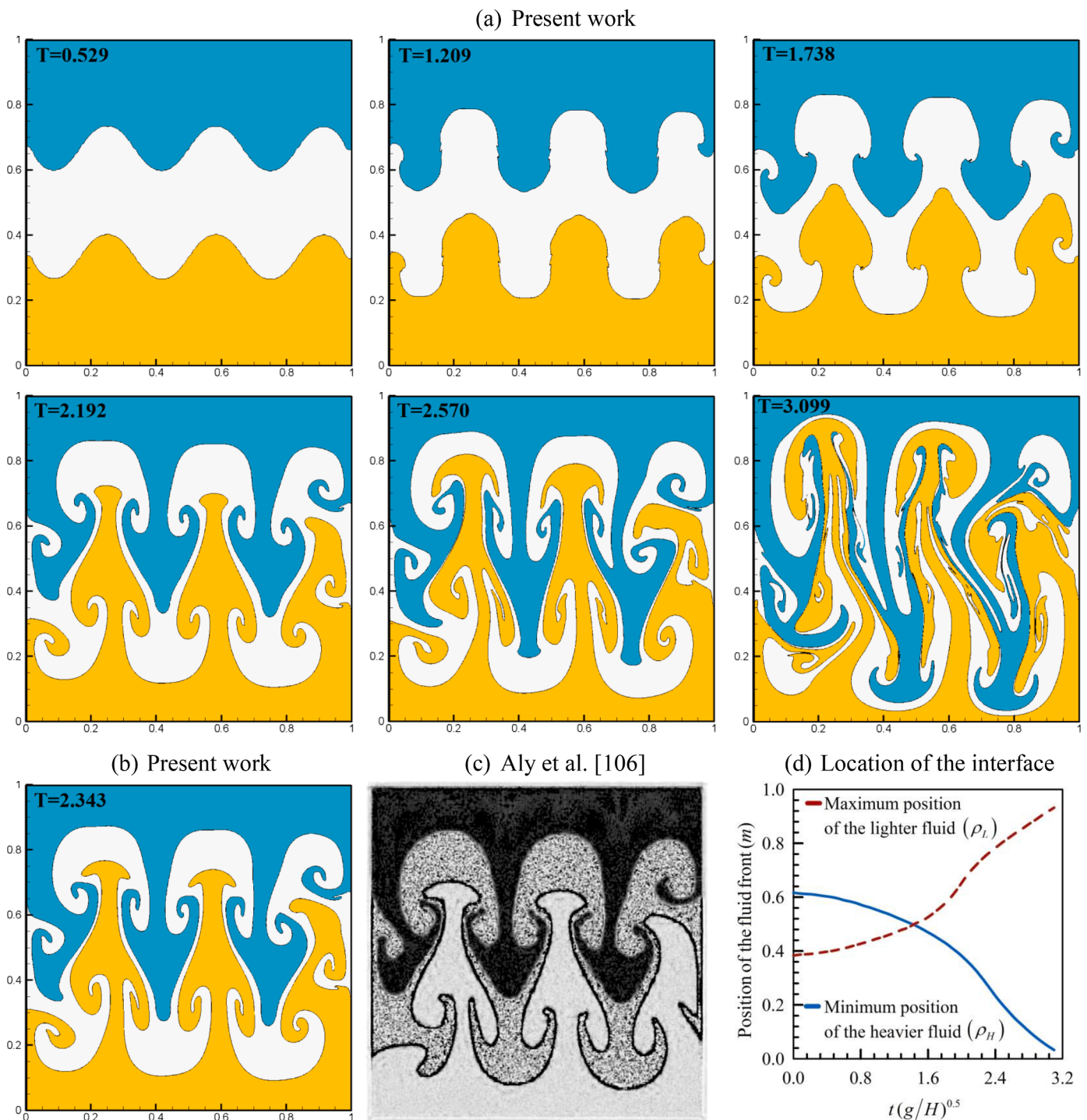


Fig. 15. (a) Time evolution of three-fluid Rayleigh-Taylor Instability (case 6) in term of the volume-fraction field calculated in the present study at different time instants, (b) and (c) qualitative comparison of the obtained result with numerical data of Aly et al. [106] at non-dimensional time of $T = t\sqrt{g/H} = 2.343$, and (d) time histories of maximum and minimum position of the interfaces (lighter (ρ_L) and heavier (ρ_H) fluids).

against a series of challenging benchmark solutions. However, as discussed earlier, the three-fluid Rayleigh-Taylor Instability can provide sufficient complexities to challenge the CFD model and assess the feasibility/reliability of open source and commercial softwares. Thus, within this section, two novel benchmark test cases will be first introduced and then analyzed using the improved VOF method, aiming to establish a foundation for the validation of existing CFD tools and to shed more light on a better understanding of transport phenomena in multi-fluid systems.

6.1. New benchmark solutions (Cases 7 and 8)

As schematically shown in Fig. 1, the computational domain is rectangular in shape with width and height of $[H, 3H]$ where $H = 1.0 \text{ m}$ stands for the referenced length. The upper, middle and lower portions of the enclosure are occupied by three immiscible Newtonian fluids with different densities ($\rho_H = 4.0 \text{ kg/m}^3$, $\rho_M = 2.0 \text{ kg/m}^3$, $\rho_L = 1.0 \text{ kg/m}^3$) and viscosities ($\mu_H = 0.04 \text{ kg/ms}$, $\mu_M = 0.02 \text{ kg/ms}$, $\mu_L = 0.01 \text{ kg/ms}$) such that $\rho_L < \rho_M < \rho_H$ and $v_L = v_M = v_H =$

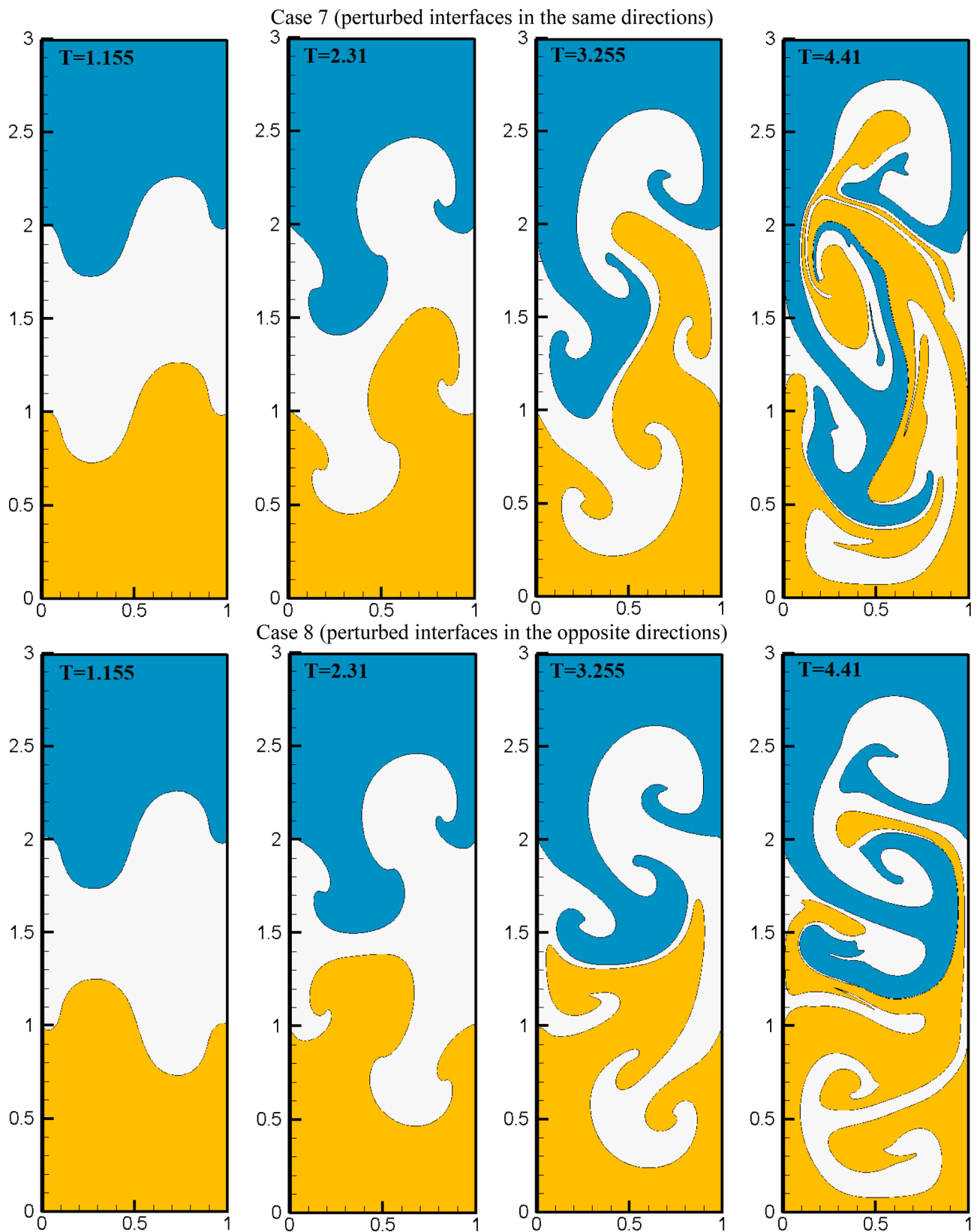


Fig. 16. Transient evolution of three-fluid Rayleigh-Taylor Instability in term of the volume-fraction field calculated in the present study at different time instants in cases 7 and 8.

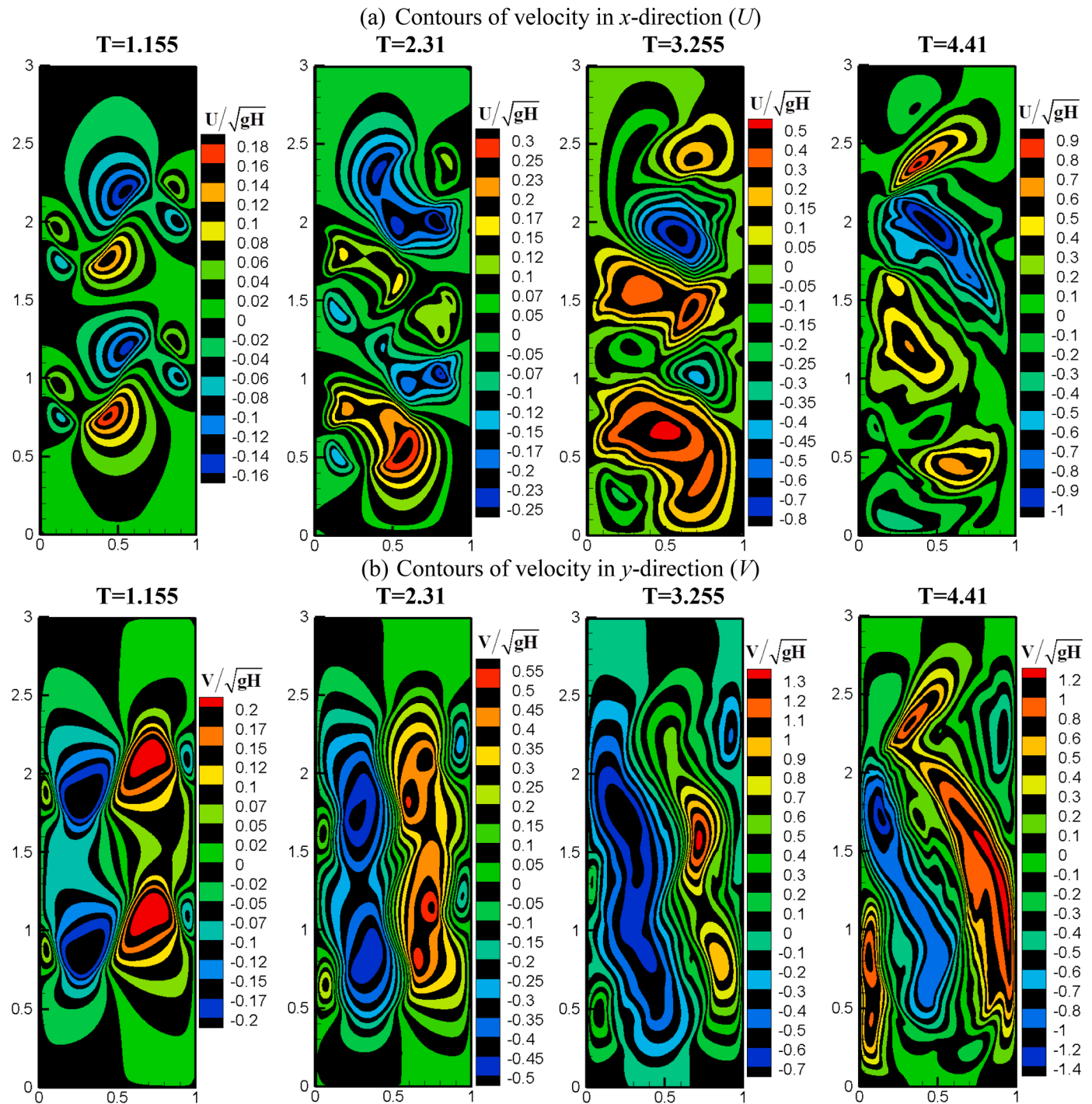


Fig. 17. Contours of non-dimensional velocity components in the x and y -directions (U, V) for three-fluid Rayleigh-Taylor Instability in case 7.

$0.01 m^2/s$ where ν_i represents the kinematic viscosity of the working fluids. The flow regime and hydrodynamic characteristics of the problems under consideration are governed by non-dimensional Atwood and Reynolds numbers defined by $At_{HL} = (\rho_H - \rho_L)/(\rho_H + \rho_L) = 3/5$ and $Re = \rho_H H \sqrt{gH}/\mu_H = 420$, respectively. Before proceeding further, it should be noted that, unlike the classical two-fluid RTI problem, in the presence of three fluids, two other Atwood numbers may be defined on the basis of two adjacent fluids namely: $At_{ML} = (\rho_M - \rho_L)/(\rho_M + \rho_L) = 1/3$ and $At_{HM} = (\rho_H - \rho_M)/(\rho_H + \rho_M) = 1/3$. Generally, at the early stages of the development, the hydrodynamic characteristics and morphological changes of the three-fluid RTI are governed by At_{ML} and At_{HM} whereas at the final stages of the evolution where high level of fluid

mixing occurs, the RTI is governed by At_{HL} . The simulations in both cases are conducted on the uniform grid resolution (300×900) and the effects of surface tension force are ignored. To initiate the instability, the interfaces between light (ρ_L), middle (ρ_M) and dense (ρ_H) fluids in cases 7 and 8 are respectively perturbed by sinusoidal functions as: disturbed interfaces in case 7

$$y_1 = 1.0 - 0.15 \times \sin(2\pi x) \quad (37)$$

$$y_2 = 2.0 - 0.15 \times \sin(2\pi x)$$

disturbed interfaces in case 8

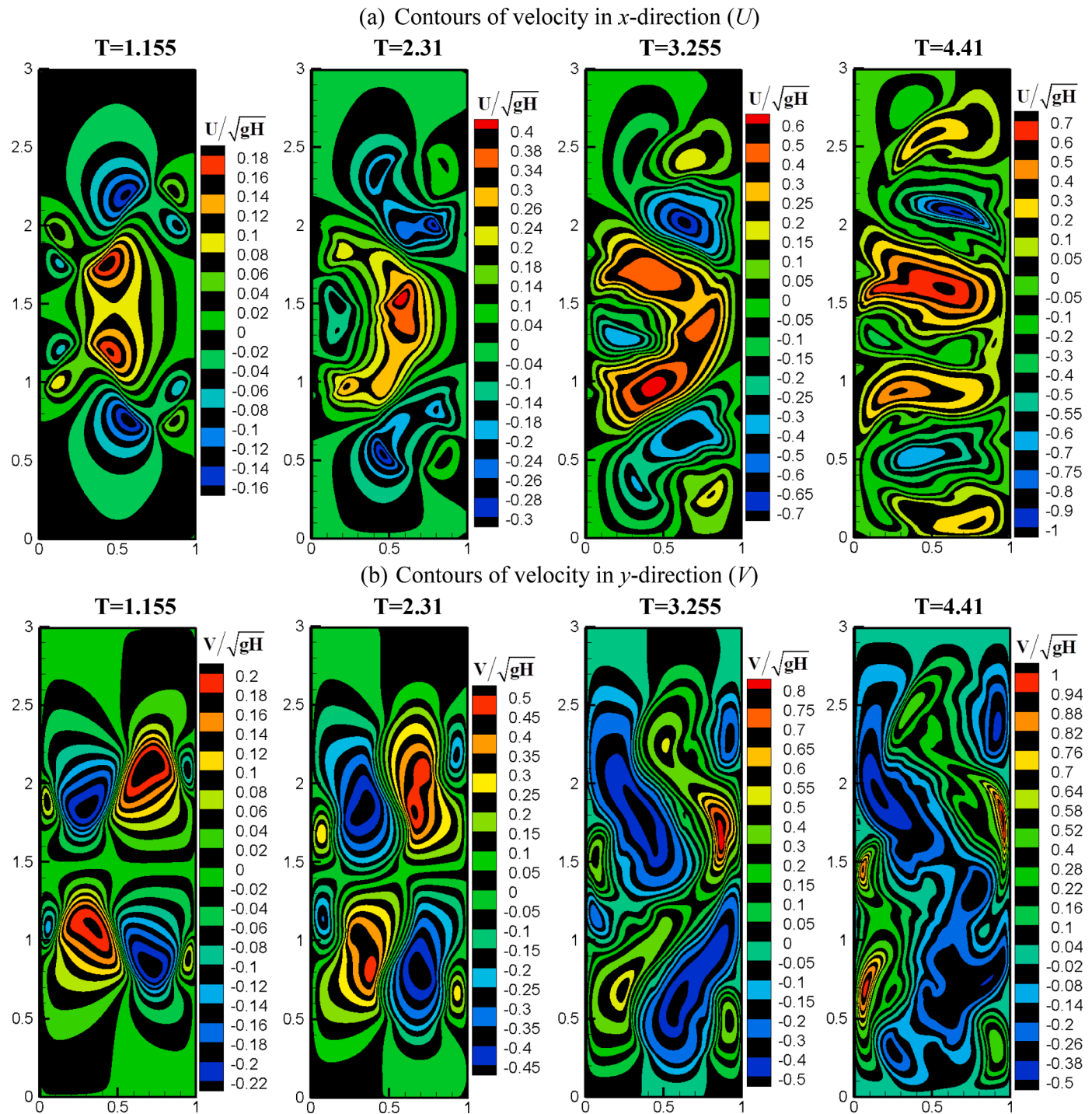


Fig. 18. Contours of non-dimensional velocity components in the x and y -directions (U, V) for three-fluid Rayleigh-Taylor Instability in case 8.

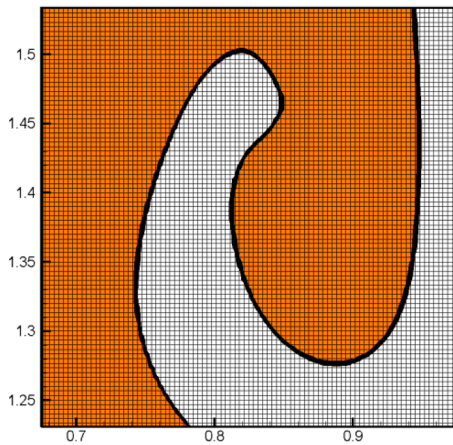
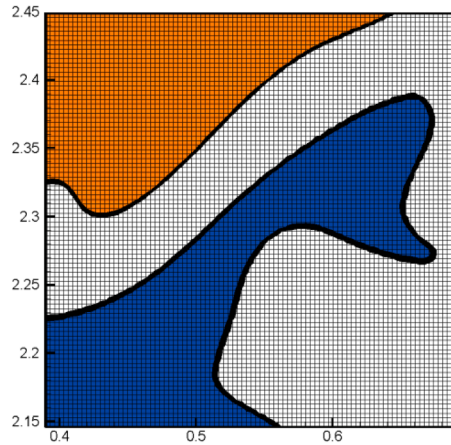
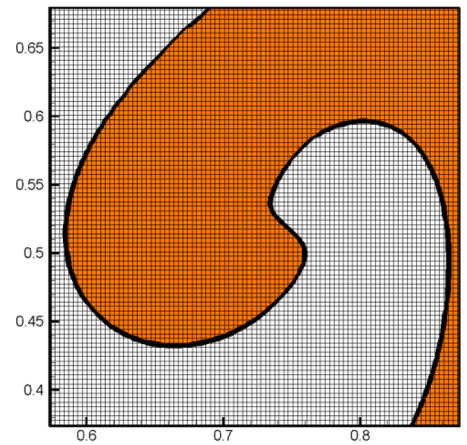
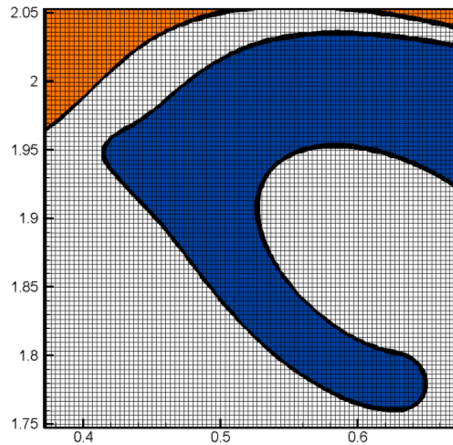
$$y_1 = 1.0 + 0.15 \times \sin(2\pi x) \quad (38)$$

$$y_2 = 2.0 - 0.15 \times \sin(2\pi x)$$

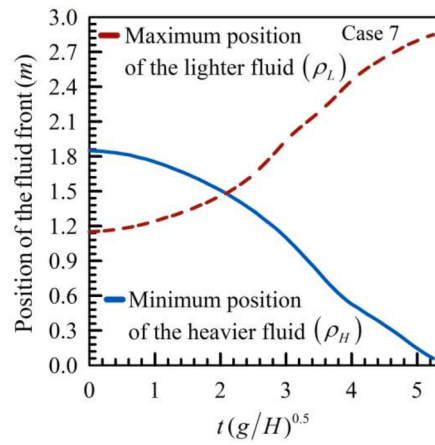
No-slip boundary condition is imposed on all rigid walls ($\mathbf{u} = 0$) and calculated results in forms of volume fraction contours and velocity fields in x - and y -directions (u, v) are displayed in Figs. 16 to 18.

Generally, regardless of the number of the fluids involved in the Rayleigh-Taylor Instability (RTI) problem, the dynamic evolution and morphological changes of this phenomenon at $At \leq 0.9$ can be categorized into three basic flow regimes namely: (1) linear, (2) weakly nonlinear (or “quasi-saturated regime”), and (3) non-linear stages [107,

110]. The linear growth regime encompasses a continuous collapse of heavy liquid and rise of less dense liquid which in turn results in the emergence of the primary and secondary vortices along the moving interfaces. Note that, in the early stage of the development, the viscous effects are negligible and only buoyancy force is leading the flow. The reversal and amplification of the initial perturbation(s) are also accompanied by the dramatic augmentation of the flow intensity and generation of shear velocity which cause the sides of the bubbles and spikes (terminology used in Refs [98,110] to distinguish the movement of the upwelling and downwelling plumes) to roll inward and become unstable to Kelvin-Helmholtz Instability (KHI) [111]. In fact, the secular growth and onset of the KHI indicate that the instability starts to enter

(a) Zoomed-in view of the interface at $T=3.255$ in case 7(b) Zoomed-in view of the interface at $T=4.41$ in case 7(c) Zoomed-in view of the interface at $T=3.255$ in case 8(d) Zoomed-in view of the interface at $T=4.41$ in case 8

(e) Position of the interfaces in case 7



(f) Position of the interfaces in case 8

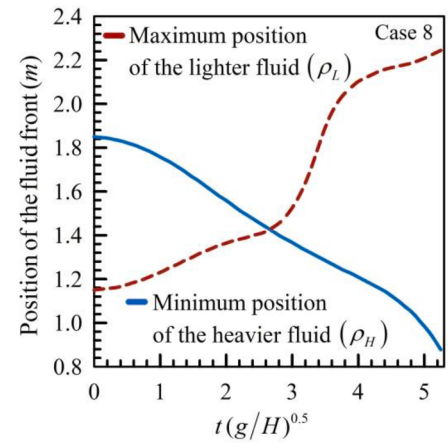


Fig. 19. (a) to (d) Zoomed-in view of the interfaces at two different non-dimensional time instants in cases 7 and 8, (e) and (f) the time histories of maximum and minimum positions of the heavier (ρ_H) and lighter (ρ_L) fluids computed in the present study in cases 7 and 8.

the weakly nonlinear dynamic and consequently the effects of viscous force become more prominent. This mechanism which manifests itself through the formation of some streamwise vortices with different wavelength is also responsible for the remarkable distortion and twisting of the material interfaces. Towards the end of the evolution, due to the interaction among the secondary eddies, the rising/falling velocity of plumes decelerates and subsequently the intensity of the fluid flow remains almost unchanged which suggest that the RTI has reached its terminal velocity and transformed to the chaotic stage.

Based on the above discussion, it can be seen from Fig. 16 that during the early stages ($0 \leq T \leq 1.155$), due to the buoyancy/gravity forces induced by density gradients across the interfaces, the heavy (ρ_H) and middle (ρ_M) fluids descend downward as spikes in the vicinity of the left wall while the middle (ρ_M) and lighter fluids (ρ_L) ascends upward in close proximity of the opposite wall to form bubbles. The corresponded contours of the velocity components in a typical (x,y) -plane in Fig. 17 show that during the process of the interactions, two counter-rotating vortices with four secondary eddies are formed inside the enclosure and remains totally symmetrical with respect to the center of the enclosure ($x = 0.5m, y = 1.5m$) which implies that the linear theory is still valid and consequently the pressure field can be estimated linearly as a function of height at equilibrium [112]. As the amplitude of the perturbations enhances ($1.155 < T \leq 2.31$), the contribution of viscous force and shear velocity to overall mass transport process increase and consequently the secondary instability (i.e. KHI) appears along the sides

of fingering structures. In fact, the formation of the mushroom-shape pattern and subsequent intensification caused by inward/outward currents are strong indications of the inception of Kelvin-Helmholtz Instability (KHI). These observations suggest that the linear theory cannot describe the asymptotic behavior of the system and the nonlinearity begins to play a role. A scrutiny of the velocity field in Fig. 17 illustrates that by this mechanism, some small inner vortices are established near and on the moving interfaces between two mixing fluids and flow intensity is invigorated in magnitude. Furthermore, it is evident that the recirculation eddies cease to be symmetric and becomes progressively amorphous. As time goes on ($2.31 < T \leq 3.255$), the spike of dense fluid and bubble of lighter fluid change their direction of motion and propagate slantly toward the centre of the container, leading to the squeeze of middle fluid and the formation of horizontal density gradients which is responsible for triggering filamentation and the elongation/branching of the interfaces. As expected, after squeezing out the interstitial fluid (ρ_M), the lighter fluid elongates longitudinally and starts to outpace and cover the heavy fluid front. The tendency of the lighter fluid to stick and surround the descending dense fluid will persist until the RTI evolution reaches its terminal condition where the magnitude of the vertical velocity component remains nearly unaltered. This phenomenon reduces the mean flow velocity and causes the blobs to spin about their centers which may occurred as a consequence of a dispersive nonlinearity. This assertion along with the reduction in mushrooming deformation of plumes structure is well supported by Figs. 16 and 17 where the

interfaces are clustered and folded into very complex shapes and magnitude of the vertical velocity component does not change significantly during the period of $3.255 < T \leq 4.41$.

However, Fig. 16 reveals that by changing the orientation of the initial interface perturbation in the lower half of the enclosure from $y_1 = 1.0 - 0.15 \times \sin(2\pi x) \text{toy}_1 = 1.0 + 0.15 \times \sin(2\pi x)$, a different scenario occurs in case 8. As expected in the early stage ($0 \leq T \leq 1.235$), the "blob" of heavy fluid sinks to the lower section of the domain whereas the light fluid rises up in the vicinity of the left wall, resulting in the formation of jet-like spikes/bubbles structure in the left half of the enclosure. Meanwhile, the contracted middle fluid penetrates simultaneously into dense and light fluids to fill the rooms that have been left by ascending/descending fluids, leading to the development of the second pair of spike-bubble interfacial shape pattern in the right half of the enclosure. Inspection of Fig. 16 together with the corresponded velocity contours in Fig. 18 illustrate that, the displacement of the interfaces and distributions of velocity components are seen to be nearly symmetric with respect to horizontal axial midline of the cavity ($y = 1.5 \text{ m}$) which conveys that the temporal evolution of the system may still be approximated within the framework of linear theory. As the RTI evolution enters the asymmetric condition and quasi-linear regime ($1.155 < T \leq 2.31$), due to the high local shear stresses and low frequency of the vortex shedding generated around the interfaces, the symmetrical Hopf bifurcation structure is gradually vanished and subsequently mushroom-shaped plume starts to emerge within the fluid domain. As the instability progresses ($2.31 < T \leq 3.255$), the intensity of the attached vortices and amplitude of the blobs enhance and consequently the appearance of Kelvin-Helmholtz type roll-up/roll-down becomes more visible. It can be seen that from Fig. 16 that, in this circumstance, the movement of the dense fluid is slightly impeded by broadening behavior of the ascending lighter fluid (ρ_L) which tends to envelop and inhibit the freely-falling liquid (ρ_H). As the dense and light fluids migrate toward the horizontal end walls ($3.255 < T \leq 4.41$), more and more secondary eddies are established within the container and the interfaces becomes quite distorted, thereby indicating that the KHI is dominant and the main flow experiences the transition from a weakly non-linear regime to a fully nonlinear one. The detailed examination of velocity contours in Fig. 18 reveals that at this stage, owing to the hydraulic balance between all relevant forces such as drag, gravity, viscosity and buoyancy, the changes in the velocity magnitude becomes nearly trivial, implying that the fluid flow approaches its terminal speed. An intriguing feature of Figs. 16 and 18 is that, due to the blockage effects of the lighter fluid in case 8, the maximum absolute value of velocity components in this case is generally lower than that of case 7.

The close-up views of the grid around the material discontinuities in Fig. 19 show that, the proposed third-order TVD flux-limiter function can efficiently suppress numerical smearing, arising from streamline-to-grid skewness and capture robustly the thin filaments and irregularities along the interfaces. It is evident that, the interface thickness between two immiscible fluids is well controlled and the color functions tend to maintain interface sharpness. The overall examination of Figs. 16 to 19 shows that both volume fraction and velocity contours in cases 7 and 8 are totally smooth across the density jumps and free of unphysical noise which in turn prove the robustness and capability of the proposed hybrid PISO-SIMPLC algorithm in satisfying continuity requirement in the convection-dominated multiphase flows with complex interface deformation. The time histories of the maximum and minimum positions of the fluid-fluid displacement fronts are plotted in Fig. 19. Careful inspection of the fluid front profiles reveals that, the lowest rate of fluid displacement occurs in case 8 which may be attributed to the aforementioned fluid trapping phenomenon and the appearance of the stagnation point in this case. That is to say, the dense and lighter fluids in case 8 meet each other at $T=2.66$ ($y=1.424 \text{ m}$) whereas this event takes place at $T=2.09$ in case 7 approximately at the central zone ($y=1.480 \text{ m}$). In addition, owing to the impeding effects of the rising lighter fluid in case 8, the heavy (H) and light (L) fluids cannot easily circulate/

distribute within the enclosure so that at the end of the simulation their global or local extrema are marked around $y_{\min,H} = 0.877 \text{ m}$ and $y_{\max,L} = 2.244 \text{ m}$ whereas these values in case 7 are $y_{\min,H} = 0.058 \text{ m}$ and $y_{\max,L} = 2.849 \text{ m}$, respectively.

Conclusion

In the present work, an improved version of the VOF method was first introduced and then exploited to simulate a series of challenging multi-fluid flow problems. To this end, a novel third-order bounded advection scheme is first derived based on the hybrid TVD-NDV constraints (Total-Variation Diminishing & Normalized Variable Diagram) and then employed for the discretization of the convection terms in the governing equations. To mitigate unfavorable effects of velocity/pressure oscillations across the density discontinuities and to speed up the convergence rate of the calculations in the incompressible multiphase flows, a novel pressure-based approach was designed via the combination of the two classical PISO and SIMPLC algorithms and then was used to fulfill the strict continuity condition and solve Pressure-Poisson Equation (PDE) on the staggered grid arrangement. Furthermore, for the accurate imposition of the surface tension force, the second-order PLIC-ELVIRA technique was coded and adopted for the calculation of the interface curvature/slope. Having demonstrated the validity and versatility of the CFD code, it has been used to analyze two new benchmark solutions namely: three-fluid Rayleigh-Taylor Instability (RTI). Based on the obtained results the following conclusions may be drawn:

- The obtained results showed that, the newly developed semi-iterative PISO-SIMPLC algorithm can successfully fulfill the mass conservation and produce smoother and continuous velocity/pressure distributions across the interface when it comes to treat violent free-surface flows with breakup.
- The results vividly confirmed the capability of the proposed modifications in dealing with wide range of multi-fluid flows with interface rupture and coalescence.
- It was found that, the newly developed convection scheme can effectively control and restrict the thickness of the material discontinuities to a maximum of 2-3 grid spacing.
- The results showed that, the improved VOF model outperformed the existent conventional mesh-free model (SPH) and provides more reliable and accurate results in dealing with the multi-fluid flows with moving interfaces.
- It was found that, the traditional Lagrangian particle method (i.e. SPH) cannot accurately capture small re-circulating eddies and is also characterized by the problem so-called "smoothing error".
- It was found that, the proposed third-order TVD-NVD convection scheme can efficiently isolate the detrimental effects of smearing the discontinuity of the fluid properties across the interface and alleviate undesirable effects of false-diffusion errors.
- The numerical simulations of single bubble rising in partially filled enclosure and Rayleigh-Taylor Instability problems clearly demonstrated the versatility and accuracy of the enhanced VOF method in handling three-fluid flows with low and high density contrasts.
- The numerical simulations of dam-break flow with and without obstacle vividly confirmed the robustness and feasibility of the proposed modifications in addressing the numerical diffusion when flow-to-grid skewness is substantial.

CRediT authorship contribution statement

Faroogh Garoosi: Conceptualization, Methodology, Validation, Visualization, Writing – original draft. **Tew-Fik Mahdi:** Supervision, Funding acquisition, Validation, Writing – review & editing.

Declaration of Competing Interest

We wish to confirm that there are no known conflicts of interest associated with this publication and there has been no significant financial support for this work that could have influenced its outcome.

Acknowledgement

This research was funded, in part, by a National Science and Engineering Research Council (NSERC) Discovery Grant for the co-author Tew-Fik Mahdi, application No: RGPIN-2021-03272.

Supplementary materials

Supplementary material associated with this article can be found, in the online version, at doi:[10.1016/j.compfluid.2022.105591](https://doi.org/10.1016/j.compfluid.2022.105591).

Appendix A. (Hybrid PISO-SIMPLEC algorithm for solving pressure-velocity linked equation)

To cope with the instability issue induced by velocity-pressure coupling in incompressible fluid flow, a novel hybrid pressure-based solver is developed along this appendix by combining two classical PISO [60] and SIMPLEC (SIMPLE-Consistent) [113] algorithms, aiming to eliminate spurious temporal pressure oscillations from the computational domain and to enhance the convergence rate of implicit iteration process.

As outlined in Section 4, the convection terms in the governing equations are discretized using the newly proposed third-order TVD-NVD bounded scheme while the second-order central differencing scheme is used to approximate the diffusive spatial derivatives. Meanwhile, the backward first-order Euler scheme is utilized to represent the time derivatives ($\partial p/\partial t$). The gradients of the pressure ($\partial p/\partial x$ and $\partial p/\partial y$) are also approximated by piecewise-linear interpolation of values from neighbouring nodes located on the momentum cell faces [61]. By implementing the above differencing schemes together with the operator notation introduced by Issa [60] and Van Doormal et al. [113], the momentum equations can be transformed into a linear algebraic equation as:

$$a_{ip}\mathbf{u}_p = \sum a_{np}\mathbf{u}_{np} + S_u + S_t - A_p(p_p - p_{np}) \quad (\text{A1})$$

In the above equations, subscripts p and np represent values at the central and neighboring nodes of the computational grid while the term $\sum a_{np}\mathbf{u}_{np}$ denotes the operator which accounts for the influence of neighboring velocities surrounding node “ p ”. The coefficient a_{np} is composed by convective and diffusion conductance across cell faces where its summation over the appropriate neighbor points can produce the diagonal coefficient $a_p = \sum a_{np}$. However, by substituting the following first-order backward time discretization scheme in Eq. (A1):

$$\frac{\partial \rho \mathbf{u}}{\partial t} = \frac{(\rho \mathbf{u})_p^{n+1} - (\rho \mathbf{u})_p^n}{\Delta t} \quad (\text{A2})$$

the diagonal coefficient a_p can be rewritten as:

$$a_{ip} = a_p + \frac{\rho_p^{n+1}}{\Delta t} \Delta x \Delta y \quad (\text{A3})$$

where a_p is the central coefficient arising from the discretization of the linearized steady-state Navier-Stokes equations [114]. In Eq. (A1), the source term S_t contains contributions from the implicitly treated parts given by:

$$S_t = \frac{(\rho \mathbf{u})_p^n}{\Delta t} \Delta x \Delta y \quad (\text{A4})$$

where the previous time-level value is denoted with superscript ‘ n ’. The source term S_u in Eq. (A1) includes all the remaining body forces such as gravity and surface tension. To initiate the first part of the procedure that corresponds to the SIMPLEC algorithm, the initial guesses for the velocity components (\mathbf{u}^*) are used. Generally, the discretized momentum equation (Eq. (A1)) based on the correct velocities and pressure values (p^{n+1}) can successfully satisfy both momentum equation and the conservation of mass as [61]:

$$a_{ip}\mathbf{u}_p^{n+1} = \left(\sum a_{np}\mathbf{u}_{np}^{n+1} \right) + S_u + S_t - A_p(p_p^{n+1} - p_{np}^{n+1}) \quad (\text{A5})$$

However, since the pressure and velocity information are completely unknown, one can introduce a guessed pressure and velocity fields (p^*, \mathbf{u}^*) and substitute them into the Eq. (A1) as:

$$a_{ip}\mathbf{u}_p^{**} = \left(\sum a_{np}\mathbf{u}_{np}^* \right) + S_u + S_t - A_p(p_p^* - p_{np}^*) \quad (\text{A6})$$

Before proceeding further, it should be stressed that, all constant coefficients in Eq. (A5) including a_{np} , a_{ip} and A_p are estimated using the guessed velocity at the current time level [115]. In the above equation, \mathbf{u}^{**} is termed as predicted velocity which cannot fulfill the mass balance. By subtracting Eq. (A6) from (A5) and defining the incremental pressure and velocity variables (p' and \mathbf{u}'), the following formulations can be obtained:

$$a_{ip}(\mathbf{u}_p^{n+1} - \mathbf{u}_p^{**}) = \sum a_{np}(\mathbf{u}_{np}^{n+1} - \mathbf{u}_{np}^*) - A_p \left[(p_p^{n+1} - p_p^*) - (p_{np}^{n+1} - p_{np}^*) \right] \quad (\text{A7})$$

$$\begin{aligned} p^{n+1} &= p^* + \alpha_{p1} p' \\ \mathbf{u}^{n+1} &= \mathbf{u}^{**} + \mathbf{u}' \end{aligned} \quad (\text{A8})$$

$$a_{ip}(\mathbf{u}'_p) = \sum a_{np}(\mathbf{u}_{np}^{n+1} - \mathbf{u}_{np}^*) - A_p \left[p'_p - p'_{np} \right] \quad (\text{A9})$$

where α_{p1} stands for the first under-relaxation factor which is taken as unity in the present study. Similar to the previous work of Van Doormaal et al. [113], in order to introduce a "Consistent" approximation, the term $\sum a_{np}(\mathbf{u}'_p)$ is subtracted from both sides of Eq. (A2). This yields:

$$(a_{ip} - \sum a_{np})\mathbf{u}'_p = \sum a_{np}(\mathbf{u}_{np}^{n+1} - \mathbf{u}_{np}^* - \mathbf{u}'_p) - A_p [p'_p - p'_{np}] \quad (\text{A10})$$

For sake of simplicity, the term $\sum a_{np}(\mathbf{u}_{np}^{n+1} - \mathbf{u}_{np}^* - \mathbf{u}'_p)$ is dropped here, and this leads to following relationship:

$$(a_{ip} - \sum a_{np})\mathbf{u}'_p = -A_p [p'_p - p'_{np}] \quad (\text{A11})$$

$$\mathbf{u}'_p = -\frac{A_p}{(a_{ip} - \sum a_{np})} [p'_p - p'_{np}] = -d_{ip} [p'_p - p'_{np}] \quad (\text{A12})$$

where $d_{ip} = A_p / (a_{ip} - \sum a_{np})$. By combining the simplified form of Eq. (A12) and Eq. (A8), one can obtain:

$$\mathbf{u}_p^{n+1} = \mathbf{u}_p^{**} - d_{ip} [p'_p - p'_{np}] \quad (\text{A13})$$

Substituting Eq. (A13) into the continuity equation yields the first Pressure-Poisson Equation (PPE) for the incremental pressure, given as [61]:

$$a_{ij} P'_{ij} = a_{i+1,j} P'_{i+1,j} + a_{i-1,j} P'_{i-1,j} + a_{i,j+1} P'_{i,j+1} + a_{i,j-1} P'_{i,j-1} + b_{ij} - \left(\frac{\rho_p^{n+1} - \rho_p^n}{\Delta t \rho_p^{n+1}} \Delta x \Delta y \right) \quad (\text{A14})$$

$$a_{ij} = a_{i+1,j} + a_{i-1,j} + a_{i,j+1} + a_{i,j-1}$$

$$a_{i+1,j} = d_{i+1,j} \Delta y, \quad a_{i-1,j} = d_{i,j} \Delta y$$

$$a_{i,j+1} = d_{i,j+1} \Delta x, \quad a_{i,j-1} = d_{i,j} \Delta x$$

$$b_{ij} = u_{ij}^{**} \Delta y - u_{i+1,j}^{**} \Delta y + v_{ij}^{**} \Delta x - v_{i,j+1}^{**} \Delta x$$

where b_{ij} stands for the mass imbalance arising from the predicted velocities. Once the pressure correction equation is solved, the predicted velocity field (\mathbf{u}^{**}) can be modified using Eqs. (A8) and (A13) as:

$$\begin{aligned} \mathbf{u}_p^{n+1} &= \mathbf{u}_p^{**} - d_{ip} [p'_p - p'_{np}] \\ p^{n+1} &= p^* + \alpha_{p1} p' \end{aligned} \quad (\text{A15})$$

At this juncture, it is important to mention that, contrary to the fully-iterative version of SIMPLC, SIMPLER and PIMPLE algorithms, the iterative loop is only imposed to Eq. (A14) rather than extending it throughout the solver, making the proposed PISO-SIMPLEC algorithm more computationally efficient in comparison with traditional pressure-based solvers [33]. Note that by modifying the guessed pressure and velocity fields via Eq. (A15), the first part of the algorithm related to the classical SIMPLEC will be completed.

To begin the second phase of the methodology related to the PISO algorithm, once again we assume that, the pressure and velocity distributions computed from the previous stage still cannot ensure both the mass and the momentum constraints. Thus, the superscripts of these variables ($p^{n+1}, \mathbf{u}^{n+1}$) are replaced by ($p^{**}, \hat{\mathbf{u}}^{**}$). By substituting the semi-corrected values of p^{**} and $\hat{\mathbf{u}}^{**}$ into the Eq. (A1), the second predicted velocities (\mathbf{u}^{***}) can be obtained as:

$$\hat{a}_{ip} \mathbf{u}_p^{***} = \sum \hat{a}_{np} \hat{\mathbf{u}}_{np}^{**} + S_u + S_t - A_p (p_p^{**} - p_{np}^{**}) \quad (\text{A16})$$

On the other hand, the discretised momentum equations with second intermediate velocities (\mathbf{u}^{***}) and correct pressure field (p^{n+1}) can lead to:

$$\hat{a}_{ip} \mathbf{u}_p^{n+1} = \sum \hat{a}_{np} \mathbf{u}_{np}^{***} + S_u + S_t - A_p (p_p^{n+1} - p_{np}^{n+1}) \quad (\text{A17})$$

In the above equation, the \mathbf{u}^{n+1} is a twice-corrected velocity field which can satisfy the continuity condition rigorously ($\nabla \cdot \mathbf{u}^{n+1} = 0$). At this stage, it should be stressed that, contrary to the standard PISO algorithm, owing to the implementation of the semi-corrected velocity and pressure values in Eq. (A16), the central (a_{ip}) and neighbor (a_{np}) coefficients in this equation is replaced and updated by the new coefficients \hat{a}_{ip} and \hat{a}_{np} , respectively. Our results have revealed that, although this modification is minor, it has a notable influence on the stability and convergence rate of numerical solution in dealing with the incompressible convection-dominated flows. By subtracting Eq. (A17) from (A16) and introducing the second incremental pressure variable (p''), the following relationships can be derived:

$$\mathbf{u}^{n+1} - \mathbf{u}_p^{***} = \frac{\sum \hat{a}_{np} \mathbf{u}_{np}^{***} + S_u + S_t}{\hat{a}_{ip}} - \frac{\sum \hat{a}_{np} \hat{\mathbf{u}}_{np}^{**} + S_u + S_t}{\hat{a}_{ip}} - \frac{A_p (p_p^{n+1} - p_{np}^{n+1})}{\hat{a}_{ip}} + \frac{A_p (p_p^{**} - p_{np}^{**})}{\hat{a}_{ip}} \quad (\text{A18})$$

$$p^{n+1} = p^{**} + \alpha_{p2} p'' \quad (\text{A19})$$

$$\mathbf{u}^{n+1} = \mathbf{u}_p^{***} + \frac{\sum \hat{a}_{np} (\mathbf{u}_{np}^{***} - \hat{\mathbf{u}}_{np}^{**})}{\hat{a}_{ip}} - \frac{A_p (p''_p - p''_{np})}{\hat{a}_{ip}} \quad (\text{A20})$$

where $\alpha_{p2} = 1$ is the second under-relaxation factor. Substitution of \mathbf{u}^{n+1} in the discretized continuity equation yields the second PPE for the incremental pressure as:

$$a_{ij} P''_{ij} = a_{i+1,j} P''_{i+1,j} + a_{i-1,j} P''_{i-1,j} + a_{i,j+1} P''_{i,j+1} + a_{i,j-1} P''_{i,j-1} + \hat{b}_{ij} + \hat{\tilde{b}}_{ij} - \frac{\rho_p^{n+1} - \rho_p^n}{\Delta t \rho_p^{n+1}} \Delta x \Delta y \quad (\text{A21})$$

$$\begin{aligned} a_{i,j} &= a_{i+1,j} + a_{i-1,j} + a_{i,j+1} + a_{i,j-1} \\ a_{i+1,j} &= d_{i+1,j} \Delta y, \quad a_{i-1,j} = d_{i,j} \Delta y \\ a_{i,j+1} &= d_{i,j+1} \Delta x, \quad a_{i,j-1} = d_{i,j} \Delta x \\ \hat{b}_{ij} &= u_{i,j}^{***} \Delta y - u_{i+1,j}^{**} \Delta y + v_{i,j}^{**} \Delta x - v_{i,j+1}^{**} \Delta x \\ \hat{\tilde{b}}_{ij} &= \left(\sum_{a_{ip}} a_{np} (u_{np}^{**} - u_{np}^{**}) \right)_{i,j} \Delta y - \left(\sum_{a_{ip}} a_{np} (u_{np}^{**} - u_{np}^{**}) \right)_{i+1,j} \Delta y \\ &+ \underbrace{\sum_{a_{ip}} a_{np} (\hat{v}_{np}^{**} - \hat{v}_{np}^{**})}_{a_{ip}}_{i,j} \Delta x - \underbrace{\sum_{a_{ip}} a_{np} (\hat{v}_{np}^{**} - \hat{v}_{np}^{**})}_{a_{ip}}_{i,j+1} \Delta x \end{aligned} \quad (\text{A22})$$

Once the second pressure correction equation is solved, the twice-corrected pressure and velocity fields can be computed via Eqs. (A19) and (A20). Having determined the correct velocity field, the volume fraction equations are solved and simulations are then transferred to the next time step where the updated physical quantities ($p^{n+1}, \mathbf{u}^{n+1}$) will be used as an initial guess values for the next level. However, before terminating this discussion, it should be noted that, in the standard PISO-algorithm, Issa [60] ideally assumed that the second intermediate velocities (\mathbf{u}^{***}) appeared as a source term (\hat{b}_{ij}) on the right hand side of Eq. (A22) is sufficiently accurate to satisfy continuity ($\nabla \cdot \mathbf{u}^{**} = 0, \hat{b}_{ij} = 0$). However, our results show that this assumption is not necessarily valid in highly nonlinear multiphase problems so that the strict enforcement of the continuity constraint via the direct imposition of $\nabla \cdot \mathbf{u}^{***} = 0$ (or $\hat{b}_{ij} = 0$) in Eq. (A22) may result in spurious pressure/velocity oscillation.

References

- [1] Tryggvason G, Scardovelli R, Zaleski S. Direct numerical simulations of gas–liquid multiphase flows. Cambridge university press; 2011.
- [2] Silvi LD, Chandraker DK, Ghosh S, Das AK. Understanding dry-out mechanism in rod bundles of boiling water reactor. Int J Heat Mass Transf 2021;177:121534.
- [3] Chen B, Fraga B, Hemida H. Large-Eddy simulation of enhanced mixing with buoyant plumes. Chem Eng Res Des 2022;177:394–405.
- [4] Ling K, Tao W-Q. A sharp-interface model coupling VOSET and IBM for simulations on melting and solidification. Comput Fluids 2019;178:113–31.
- [5] Mallya N, Haussener S. Buoyancy-driven melting and solidification heat transfer analysis in encapsulated phase change materials. Int J Heat Mass Transf 2021;164:120525.
- [6] Li X, Hao Y, Zhao P, Fan M, Song S. Simulation study on the phase holdup characteristics of the gas–liquid–solid mini-fluidized beds with bubbling flow. Chem Eng J 2022;427:131488.
- [7] Pezo ML, Pezo L, Dragojlović D, Čolović R, Čolović D, Vidosavljević S, Hadnadev M, Đuragić O. Experimental and computational study of the two-fluid nozzle spreading characteristics. Chem Eng Res Des 2021;166:18–28.
- [8] Tretola G, Vogiatzaki K, Navarro-Martinez S. Implementation of a probabilistic surface density volume of fluid approach for spray atomisation. Comput Fluids 2021;105121.
- [9] Kan K, Chen H, Zheng Y, Zhou D, Binama M, Dai J. Transient characteristics during power-off process in a shaft extension tubular pump by using a suitable numerical model. Renew Energy 2021;164:109–21.
- [10] Shrestha K, Salati H, Fletcher D, Singh N, Inthavong K. Effects of head tilt on squeeze-bottle nasal irrigation—a computational fluid dynamics study. J Biomech 2021;123:110490.
- [11] Sarker S, Chatzizisis YS, Terry BS. Computational optimization of a novel atrumatic catheter for local drug delivery in coronary atherosclerotic plaques. Med Eng Phys 2020;79:26–32.
- [12] Tu J, Yeoh GH, Liu C. Computational fluid dynamics: a practical approach. Butterworth-Heinemann; 2018.
- [13] Bureš L, Sato Y. Direct numerical simulation of evaporation and condensation with the geometric VOF method and a sharp-interface phase-change model. Int J Heat Mass Transf 2021;173:121233.
- [14] Sussman M, Smereka P, Osher S. A level set approach for computing solutions to incompressible two-phase flow. J Comput Phys 1994;114:146–59.
- [15] Hirt CW, Nichols BD. Volume of fluid (VOF) method for the dynamics of free boundaries. J Comput Phys 1981;39:201–25.
- [16] Attili T, Heller V, Triantafyllou S. A numerical investigation of tsunamis impacting dams. Coast Eng 2021:103942.
- [17] Liu F, Xu Y, Li Y. A coupled level-set and Volume-Of-Fluid method for simulating axi-symmetric incompressible two-phase flows. Appl Math Comput 2017;293:112–30.
- [18] He M, Wang S-P, Ren S-F, Zhang S. Numerical study of effects of stand-off distance and gravity on large scale bubbles near a breach. Appl Ocean Res 2021;117:102946.
- [19] Antepara O, Balcázar N, Rigola J, Oliva A. Numerical study of rising bubbles with path instability using conservative level-set and adaptive mesh refinement. Comput Fluids 2019;187:83–97.
- [20] Issakhov A, Borsikbayeva A. The impact of a multilevel protection column on the propagation of a water wave and pressure distribution during a dam break: Numerical simulation. J Hydrol 2021;598:126212.
- [21] Liu W, Wang B, Guo Y. Numerical study of the dam-break waves and Favre waves down sloped wet rigid-bed at laboratory scale. J Hydrol 2021;602:126752.
- [22] Gu ZH, Wen HL, Yu CH, Sheu TWH. Interface-preserving level set method for simulating dam-break flows. J Comput Phys 2018;374:249–80.
- [23] Hanene Z, Alla H, Abdelouhab M, Roques-Carmes T. A numerical model of an immiscible surfactant drop spreading over thin liquid layers using CFD/VOF approach. Colloids Surf A Physicochem Eng Asp 2020;600:124953.
- [24] Zeng C, Deng W, Fan J, Zhang Y. Effect of flow profiles on the flow subjected to oscillation forcing: an example of droplet mobilization in constricted tubes. J Hydrol 2020;583:124295.
- [25] Di Paolo B, Lara JL, Barajas G, Losada IJ. Wave and structure interaction using multi-domain couplings for Navier-Stokes solvers in OpenFOAM®. Part I: implementation and validation. Coast Eng 2021;164:103799.
- [26] Booshi S, Katabdari MJ. Modeling of solitary wave interaction with emerged porous breakwater using PLIC-VOF method. Ocean Eng 2021;241:110041.
- [27] Jafari E, Namin MM, Badie P. Numerical simulation of wave interaction with porous structures. Appl Ocean Res 2021;108:102522.
- [28] Saye RI, Sethian JA. A review of level set methods to model interfaces moving under complex physics: recent challenges and advances. Handbook of numerical analysis. Elsevier; 2020. p. 509–54.
- [29] Marić T, Kothe DB, Bothe D. Unstructured un-split geometrical Volume-Of-Fluid methods—a review. J Comput Phys 2020;420:109695.
- [30] Zuzio D, Orazzo A, Estivalèzes J-L, Lagrange I. A new efficient momentum preserving level-set/vof method for high density and momentum ratio incompressible two-phase flows. J Comput Phys 2020;410:109342.
- [31] Gibou F, Hyde D, Fedkiw R. Sharp interface approaches and deep learning techniques for multiphase flows. J Comput Phys 2019;380:442–63.
- [32] Scapin N, Costa P, Brandt L. A Volume-Of-Fluid method for interface-resolved simulations of phase-changing two-fluid flows. J Comput Phys 2020;407:109251.
- [33] Wang H, Wang H, Gao F, Zhou P, Zhai ZJ. Literature review on pressure–velocity decoupling algorithms applied to built-environment CFD simulation. Build Environ 2018;143:671–8.
- [34] Kumar R, Cheng L, Xiong Y, Xie B, Abgrall R, Xiao F. THINC scaling method that bridges VOF and level set schemes. J Comput Phys 2021;436:110323.
- [35] Pilliod Jr JE, Puckett EG. Second-order accurate Volume-Of-Fluid algorithms for tracking material interfaces. J Comput Phys 2004;199:465–502.
- [36] Gaskell PH, Lau A. Curvature-compensated convective transport: SMART, a new boundedness-preserving transport algorithm. Int J Numer Methods Fluids 1988;8:617–41.
- [37] Leonard BP. Simple high-accuracy resolution program for convective modelling of discontinuities. Int J Numer Methods Fluids 1988;8:1291–318.
- [38] Harten A. High resolution schemes for hyperbolic conservation laws. J Comput Phys 1997;135:260–78.
- [39] Sweby PK. High resolution schemes using flux limiters for hyperbolic conservation laws. SIAM J Numer Anal 1984;21:995–1011.

- [40] Lin C-H, Lin CA. Simple high-order bounded convection scheme to model discontinuities. *AIAA J* 1997;35:563–5.
- [41] Alves MA, Oliveira PJ, Pinho FT. A convergent and universally bounded interpolation scheme for the treatment of advection. *Int J Numer Methods Fluids* 2003;41:47–75.
- [42] Chourashi T. A High Resolution Equi-Gradient scheme for convective flows. *Appl Math Comput* 2018;338:123–40.
- [43] Lima GAB, Ferreira VG, Cirilo ER, Castelo A, Candezano MAC, Tasso IVM, Sano DMC, de A. Scalvi LV. A continuously differentiable upwinding scheme for the simulation of fluid flow problems. *Appl Math Comput* 2012;218:8614–33.
- [44] Gao W, Li H, Liu Y. A high resolution NV/TVD Hermite polynomial upwind scheme for convection-dominated problems. *Math Methods Appl Sci* 2013;36: 1107–22.
- [45] Choi SK, Nam HY, Cho M. A comparison of higher-order bounded convection schemes. *Comput Methods Appl Mech Eng* 1995;121:281–301.
- [46] Ubbink O, Issa RI. A method for capturing sharp fluid interfaces on arbitrary meshes. *J Comput Phys* 1999;153:26–50.
- [47] Gopala VR, van Wachem BGM. Volume of fluid methods for immiscible-fluid and free-surface flows. *Chem Eng J* 2008;141:204–21.
- [48] Zhang D, Jiang C, Liang D, Chen Z, Yang Y, Shi Y. A refined Volume-Of-Fluid algorithm for capturing sharp fluid interfaces on arbitrary meshes. *J Comput Phys* 2014;274:709–36.
- [49] Nguyen V-T, Park W-G. A Volume-Of-Fluid (VOF) interface-sharpening method for two-phase incompressible flows. *Comput Fluids* 2017;152:104–19.
- [50] Waclawczyk T, Koronowicz T. Comparison of CICSAM and HRIC high-resolution schemes for interface capturing. *J. Theor. Appl. Mech.* 2008;46:325–45.
- [51] Heyns JA, Malan AG, Harms TM, Oxtoby OF. Development of a compressive surface capturing formulation for modelling free-surface flow by using the Volume-Of-Fluid approach. *Int J Numer Methods Fluids* 2013;71:788–804.
- [52] Cifani P, Michalek WR, Priems GJM, Kuerten JGM, van der Geld CWM, Geurts BJ. A comparison between the surface compression method and an interface reconstruction method for the VOF approach. *Comput Fluids* 2016;136:421–35.
- [53] Zanotto CP, Paladino EE, Evrard F, van Wachem B, Denner F. Modeling of interfacial mass transfer based on a single-field formulation and an algebraic VOF method considering non-isothermal systems and large volume changes. *Chem Eng Sci* 2022;247:116855.
- [54] Akhlaghi M, Mohammadi V, Nouri NM, Taherkhani M, Karimi M. Multi-fluid VoF model assessment to simulate the horizontal air-water intermittent flow. *Chem Eng Res Des* 2019;152:48–59.
- [55] Peng Z, Ge L, Moreno-Atanasio R, Evans G, Moghtaderi B, Doroodchi E. VOF-DEM study of solid distribution characteristics in slurry taylor flow-based multiphase microreactors. *Chem Eng J* 2020;396:124738.
- [56] Habchi C, Russeil S, Bougeard D, Harion J-L, Lemenand T, Ghanem A, Della Valle D, Peerhossaini H. Partitioned solver for strongly coupled fluid-structure interaction. *Comput Fluids* 2013;71:306–19.
- [57] Sarah R, Jayakumar JS. Study of bubble dynamics in aerated liquid storage tanks opened to atmosphere. *Advances in thermofluids and renewable energy*. Springer; 2022. p. 175–90.
- [58] Introini C, Lorenzi S, Cammi A, Baroli D, Peters B, Bordas S. A mass conservative Kalman filter algorithm for computational thermo-fluid dynamics. *Materials (Basel)* 2018;11:2222.
- [59] Kim S, Oshima N, Park HJ, Murai Y. Direct numerical simulation of frictional drag modulation in horizontal channel flow subjected to single large-sized bubble injection. *Int J Multiph Flow* 2021;145:103838.
- [60] Issa RI. Solution of the implicitly discretised fluid flow equations by operator-splitting. *J Comput Phys* 1986;62:40–65.
- [61] Versteeg HK, Malalasekera W. An introduction to computational fluid dynamics: the finite volume method. Pearson Education; 2007.
- [62] Youngs DL. Time-dependent multi-material flow with large fluid distortion. *Numer Methods Fluid Dyn* 1982;24:273–85.
- [63] Garoosi F, Mahdi T. Presenting a novel higher-order bounded convection scheme for simulation of multiphase flows and convection heat transfer. *Int J Heat Mass Transf* 2021;172:121163.
- [64] Puckett EG, Almgren AS, Bell JB, Marcus DL, Rider WJ. A high-order projection method for tracking fluid interfaces in variable density incompressible flows. *J Comput Phys* 1997;130:269–82.
- [65] Soh GY, Yeoh GH, Timchenko V. An algorithm to calculate interfacial area for multiphase mass transfer through the Volume-Of-Fluid method. *Int J Heat Mass Transf* 2016;100:573–81.
- [66] Brackbill JU, Kothe DB, Zemach C. A continuum method for modeling surface tension. *J Comput Phys* 1992;100:335–54.
- [67] Yin X, Zarikos I, Karadimitriou NK, Raof A, Hassanzadeh SM. Direct simulations of two-phase flow experiments of different geometry complexities using Volume-Of-Fluid (VOF) method. *Chem Eng Sci* 2019;195:820–7.
- [68] Cerqueira RFL, Paladino EE, Evrard F, Denner F, van Wachem B. Multiscale modeling and validation of the flow around Taylor bubbles surrounded with small dispersed bubbles using a coupled VOF-DBM approach. *Int J Multiph Flow* 2021;141:103673.
- [69] Zijlema M. On the construction of a third-order accurate monotone convection scheme with application to turbulent flows in general domains. *Int J Numer Methods Fluids* 1996;22:619–41.
- [70] Bidadi S, Rani SL. Quantification of numerical diffusivity due to TVD schemes in the advection equation. *J Comput Phys* 2014;261:65–82.
- [71] Van Leer B. Towards the ultimate conservative difference scheme. V. A second-order sequel to Godunov's method. *J Comput Phys* 1979;32:101–36.
- [72] Van Leer B. Towards the ultimate conservative difference scheme. II. Monotonicity and conservation combined in a second-order scheme. *J Comput Phys* 1974;14:361–70.
- [73] Gao W, Li H, Liu Y, Jian Y-J. An oscillation-free high order TVD/CBC-based upwind scheme for convection discretization. *Numer Algorithms* 2012;59:29–50.
- [74] Darwish MS, Moukalled FH. Normalized variable and space formulation methodology for high-resolution schemes. *Numer Heat Transf* 1994;26:79–96.
- [75] Martin JC, Moyce WJ, Part IV. An experimental study of the collapse of liquid columns on a rigid horizontal plane. *Philos. Trans. R. Soc. London. Ser. A, Math. Phys. Sci.* 1952;244:312–24.
- [76] Ling K, Zhang S, Wu P-Z, Yang S-Y, Tao W-Q. A coupled Volume-Of-Fluid and level-set method (VOSET) for capturing interface of two-phase flows in arbitrary polygon grid. *Int J Heat Mass Transf* 2019;143:118565.
- [77] Sheu TWH, Yu C-H, Chiu P-H. Development of a dispersively accurate conservative level set scheme for capturing interface in two-phase flows. *J Comput Phys* 2009;228:661–86.
- [78] Xu X, Jiang YL, Yu P. SPH simulations of 3D dam-break flow against various forms of the obstacle: toward an optimal design. *Ocean Eng* 2021;229:108978.
- [79] Colagrossi A, Landrini M. Numerical simulation of interfacial flows by smoothed particle hydrodynamics. *J Comput Phys* 2003;191:448–75.
- [80] Li Y, Raichlen F. Energy balance model for breaking solitary wave runup. *J Waterw Port, Coastal, Ocean Eng* 2003;129:47–59.
- [81] Koshizuka S, Oka Y, Tamako H. A particle method for calculating splashing of incompressible viscous fluid. *La Grange Park, IL (United States: American Nuclear Society, Inc.); 1995*.
- [82] Hänsch S, Lucas D, Höhne T, Krepper E. Application of a new concept for multi-scale interfacial structures to the dam-break case with an obstacle. *Nucl Eng Des* 2014;279:171–81.
- [83] Issakhov A, Zhandaulet Y, Nogaeva A. Numerical simulation of dam break flow for various forms of the obstacle by VOF method. *Int J Multiph Flow* 2018;109: 191–206.
- [84] Peng Y-X, Zhang A-M, Wang S-P. Coupling of WCSPH and RKPM for the simulation of incompressible fluid-structure interactions. *J Fluids Struct* 2021; 102:103254.
- [85] Lin C, Hwang H-H. External and internal flow fields of plunging breakers. *Exp Fluids* 1992;12:229–37.
- [86] Pan D, Chang C. The capturing of free surfaces in incompressible multi-fluid flows. *Int J Numer Methods Fluids* 2000;33:203–22.
- [87] Ming FR, Sun PN, Zhang AM. Numerical investigation of rising bubbles bursting at a free surface through a multiphase SPH model. *Mechanica* 2017;52:2665–84.
- [88] Li HY, Yap YF, Lou J, Shang Z. Numerical modelling of three-fluid flow using the level-set method. *Chem Eng Sci* 2015;126:224–36.
- [89] Zhao Y, Tan HH, Zhang B. A high-resolution characteristics-based implicit dual time-stepping VOF method for free surface flow simulation on unstructured grids. *J Comput Phys* 2002;183:233–73.
- [90] Cummins SJ, Rudman M. An SPH projection method. *J Comput Phys* 1999;152: 584–607.
- [91] Shadloo MS, Zainali A, Yildiz M. Simulation of single mode Rayleigh–Taylor instability by SPH method. *Comput Mech* 2013;51:699–715.
- [92] Schilling O. Progress on understanding Rayleigh–Taylor flow and mixing using synergy between simulation, modeling, and experiment. *J Fluids Eng* 2020;142: 120802.
- [93] Banerjee A. Rayleigh–Taylor Instability: A status review of experimental designs and measurement diagnostics. *J Fluids Eng* 2020;142:120801.
- [94] Boffetta G, Mazzino A. Incompressible rayleigh–taylor turbulence. *Annu Rev Fluid Mech* 2017;49:119–43.
- [95] Pahar G, Dhar A. Mixed miscible-immiscible fluid flow modelling with incompressible SPH framework. *Eng Anal Bound Elem* 2016;73:50–60.
- [96] Garoosi F, Shakibaeinia A. Numerical simulation of Rayleigh–Bénard convection and three-phase Rayleigh–Taylor instability using a modified MPS method. *Eng Anal Bound Elem* 2021;123:1–35.
- [97] Rezavand M, Taebi-Rahni M, Rauch W. An ISPH scheme for numerical simulation of multiphase flows with complex interfaces and high density ratios. *Comput Math Appl* 2018;75:2658–77.
- [98] Celani A, Mazzino A, Muratore-Ginanneschi P, Vozella L. Phase-field model for the Rayleigh–Taylor instability of immiscible fluids. *J Fluid Mech* 2009;622: 115–34.
- [99] Talat N, Mavrić B, Hatić V, Bajt S, Šarler B. Phase field simulation of Rayleigh–Taylor instability with a meshless method. *Eng Anal Bound Elem* 2018; 87:78–89.
- [100] Luo T, Wang J, Xie C, Wan M, Chen S. Effects of compressibility and Atwood number on the single-mode Rayleigh–Taylor instability. *Phys Fluids* 2020;32: 12110.
- [101] Luo T, Wang J. Effects of Atwood number and stratification parameter on compressible multi-mode Rayleigh–Taylor instability. *Phys Fluids* 2021;33: 115111.
- [102] Garoosi F, Shakibaeinia A. An improved high-order ISPH method for simulation of free-surface flows and convection heat transfer. *Powder Technol* 2020;376: 668–96.
- [103] Agertz O, Moore B, Stadel J, Potter D, Miniati F, Read J, Mayer L, Gawryszczak A, Kravtsov A, Nordlund Å. Fundamental differences between SPH and grid methods. *Mon Not R Astron Soc* 2007;380:963–78.
- [104] Bender J, Koschier D, Kugelstadt T, Weiler M. Turbulent micropolar SPH fluids with foam. *IEEE Trans Vis Comput Graph* 2018;25:2284–95.

- [105] Sun PN, Colagrossi A, Marrone S, Antuono M, Zhang AM. Multi-resolution Delta-plus-SPH with tensile instability control: towards high Reynolds number flows. *Comput Phys Commun* 2018;224:63–80.
- [106] Aly AM. Modeling of multi-phase flows and natural convection in a square cavity using an incompressible smoothed particle hydrodynamics. *Int J Numer Methods Heat Fluid Flow* 2015;25:513–33.
- [107] Tryggvason G. Numerical simulations of the Rayleigh-Taylor instability. *J Comput Phys* 1988;75:253–82.
- [108] Garoosi F, Shakibaenia A. Numerical simulation of free-surface flow and convection heat transfer using a modified Weakly Compressible Smoothed Particle Hydrodynamics (WCSPH) method. *Int J Mech Sci* 2020;188:105940.
- [109] Trask N, Maxey M, Kim K, Perego M, Parks ML, Yang K, Xu J. A scalable consistent second-order SPH solver for unsteady low Reynolds number flows. *Comput Methods Appl Mech Eng* 2015;289:155–78.
- [110] He X, Chen S, Zhang R. A lattice Boltzmann scheme for incompressible multiphase flow and its application in simulation of Rayleigh-Taylor instability. *J Comput Phys* 1999;152:642–63.
- [111] Daly BJ. Numerical study of two fluid Rayleigh-Taylor instability. *Phys Fluids* 1967;10:297–307.
- [112] Zhang Q. The motion of a single bubble or spike in Rayleigh-Taylor unstable interfaces, IMPACT. *Comput Sci Eng* 1991;3:277–304.
- [113] Van Doormaal JP, Raithby GD. Enhancements of the SIMPLE method for predicting incompressible fluid flows. *Numer Heat Transf* 1984;7:147–63.
- [114] Tuković Ž, Perić M, Jasak H. Consistent second-order time-accurate non-iterative PISO-algorithm. *Comput Fluids* 2018;166:78–85.
- [115] MacNamara S, Strang G. Operator splitting. Splitting methods in communication imaging, science and engineering. Springer; 2016. p. 95–114.